DIPLOMARBEIT

Load dependence of the *ab-initio* real contact area

zur Erlangung des akademischen Grades

Diplom-Ingenieur

im Rahmen des Studiums

Technische Physik

eingereicht von

Florian Buchner
Matrikelnummer 01325815

ausgeführt am Institut für Angewandte Physik
der Fakultät für Technische Physik der Technischen Universität Wien
in Zusammenarbeit mit AC2T research GmbH

Betreuung
Betreuer: Privatdoz. Dr.rer.nat. András Vernes
Zweitbetreuer: Univ.Prof. Dipl.-Ing. Dr.techn. Markus Valtiner

Wien, 16. Oktober 2020

Unterschrift Verfasser

Unterschrift Betreuer

Abstract

The real area of contact between two bodies is a quantity of great interest in (nano-)tribology, due to its central role in phenomena like friction, wear and adhesion. Of particular relevance is how it depends on the load pressing the two bodies together. For estimation, models from continuum mechanics are commonly used. However, their applicability is questionable as the atomic scale is approached.

To shed light on this, we revisit an earlier work by Wolloch *et al.* [Phys. Rev. B 91, 195436]. Therein, a theoretical model for the *ab-initio* definition and calculation of contact areas on the atomic scale has been proposed and applied to an atomic force microscope (AFM) system consisting of a tungsten tip and a graphene layer on an iridium substrate. For the necessary electronic structure calculations, density-functional theory is used.

In the past, for this AFM-system, the load dependence of the contact area was determined using only a small amount of data (system configurations). This motivated us to extend the previous investigation, firstly by generating more configurations, secondly by trying to refine the analysis method by which the load dependence is determined from the data. Furthermore, we attempt an interpretation in terms of a particular contact model from the literature that we believe is the closest continuum analog of our atomistic AFM-system. As far as the fundamental concepts are comparable, our results for the load dependence of the contact area seem approximately consistent with that obtained for the continuum model.

Kurzfassung

Die reale Kontaktfläche zwischen zwei Körpern ist eine Größe von hohem Interesse in der (Nano-)Tribologie, wegen ihrer zentralen Rolle in der Erklärung von Phänomenen wie Reibung, Verschleiß und Adhäsion. Insbesondere relevant ist ihre Abhängigkeit von der Last, mit der die beteiligten Körper aneinandergedrückt werden. Zur Abschätzung werden gewöhnlich Modelle aus der Kontinuumsmechanik verwendet. Doch deren Anwendbarkeit ist fraglich, wenn man in den Bereich atomarer Längenskalen kommt.

Zur Beleuchtung dieser Problematik greifen wir hier eine frühere Arbeit von Wolloch *et al.* [Phys. Rev. B 91, 195436] erneut auf. Darin wurde ein theoretisches Modell zur *ab-initio* Definition und Berechnung von Kontaktflächen auf atomarer Ebene vorgeschlagen, und auf ein Rasterkraftmikroskop(AFM)-Modellsystem, bestehend aus einer Wolframspitze und einer Graphenschicht auf Iridiumsubstrat, angewandt. Für die benötigten elektronischen Strukturberechnungen kommt die Dichtefunktionaltheorie zum Einsatz.

Die für dieses AFM-System gefundene Lastabhängigkeit der Kontaktfläche wurde allerdings aus der Analyse von nur wenigen Daten (Systemkonfigurationen) bestimmt. Dies veranlasste uns zu einer Erweiterung der früheren Untersuchung, indem wir erstens mehr Konfigurationen erzeugen, und zweitens auch die Analysemethode zur Extraktion der Lastabhängigkeit aus den Daten zu verfeinern versuchen. Ferner versuchen wir eine Interpretation der Ergebnisse im Hinblick auf ein spezielles Kontaktmodell aus der Literatur, das wir für das engste Kontinuums-Analogon unseres atomistischen Systems halten. Soweit die Grundbegriffe als vergleichbar gelten können, scheinen unsere Ergebnisse für die Lastabhängigkeit der Kontaktfläche im Groben zu diesem Kontinuumsmodell sehr gut zu passen.

Contents

1 Introduction

In theories of friction, wear and adhesion, part of the wide and highly interdisciplinary field of tribology, a key quantity that has been invoked to illuminate these phenomena is the area of contact between the involved bodies in contact. Closely related to this is the field of contact mechanics, which is concerned with "the stresses and deformations which arise when the surfaces of two solid bodies are brought into contact" [1].

The classical laws of friction between macroscopic bodies state that the friction force between sliding bodies is independent of their apparent (nominal) area of contact, and proportional to the load pressing them together. The latter statement is expressed as

$$F_f = \mu \cdot L \,, \tag{1.1}$$

where F_f is the friction force, L is the load, and the proportionality constant μ linking them is called the *coefficient of friction*. While it appears that Leonardo da Vinci already possessed knowledge of these laws, he did not publish his works on the subject [2]. It was not until two hundred years later that Guillaume Amontons rediscovered and published [3] these friction laws. Additional important contributions are due to Charles Augustin de Coulomb [4], who confirmed Amontons's results in a series of extensive and thorough experiments, and further noted that the friction is independent of sliding velocity, in a first-order approximation. These classical laws are empirical in their nature and for a long time lacked in a convincing explanation, especially the rather unintuitive result that the apparent contact area seems to play no role.

This was resolved by Bowden and Tabor [5, 6], who noted the necessary distinction between the *apparent* and the *real contact area*. Due to inevitable roughness on the microscale, two surfaces make contact only at the peaks or summits, known as *asperities*. This contact due to asperities results in a real contact area orders of magnitude smaller than the apparent contact area. Bowden and Tabor found experimentally that this real contact area is nearly independent of the apparent contact area and rises linearly with load. Assuming that friction is due to the shearing of the asperity junctions, and therefore proportional to the real contact area, the classical macroscale friction laws could follow. The linear load dependence of the real contact area was originally explained by plastic flow of the asperities.

Later works [7, 8] showed that purely elastic deformation, too, can produce such a behavior in multi-asperity contacts.

These results highlight the general fact that friction arises as a complex collective effect from many asperities. For a fundamental understanding, studies of isolated single-asperity contacts, under precisely controllable conditions, are needed. A review is available in Ref. [9]. A tool that allows the experimental study of single-asperity contacts is the atomic force microscope (AFM) [10]. For the study of nanoscale friction with AFM, the term of 'friction force microscope' (FFM) [11] is also common. Loosely speaking, a sharp tip attached to a compliant cantilever is dragged across a surface, while registering both the normal deflection and twisting of the cantilever, from which normal and lateral forces can be determined.

Numerous experimental FFM studies [12–18] have reported proportionality between friction force and real contact area in nanometer-sized solid-solid contacts, i.e.,

$$F_f = \tau \cdot A(L)\,, \tag{1.2}$$

as long as no wear occurs. The factor τ is called the interfacial shear strength. When the single-asperity contact area $A(L)$ nonlinearly depends on load, so does the friction $F_f(L)$, too, in contrast to the familiar macroscale behavior described by Eq. 1.1.

Since direct measurement or imaging of the contact area in FFM is hard, if not impossible, the evidence for Eq. 1.2 is only indirect. One way is to measure contact conductance, which can give information about the contact area [19]. But evidence comes mostly from comparing measured friction-vs-load curves with theoretical predictions for the load-dependent contact area $A(L)$ from continuum mechanics models. Such continuum models are a mainstay of the interpretation of FFM experiments, and they appear to describe tip-sample contacts well even at nanometer length scales. Despite this, it is hard to imagine that there will not be a point where they cease to be applicable because of atomic discreteness. Indeed, molecular-dynamics simulations have pointed out the failure of continuum models at the atomic scale [20, 21]. To test contact models at, or extend them to the atomic scale, it is necessary to first define what even constitutes contact (and contact area) in an atomistic picture. Several efforts along these lines have been made [22–25], including quite successful attempts to link atomic-level contact areas to friction [26–32].

Another example of an atomic-scale contact model is the one by M. Wolloch *et al.* [33], which the present thesis is based on. It is notable that for defining the contact in a first-principles approach based on density-functional theory, Bader's quantum theory of atoms in molecules [34] is proposed to be used, and as far as we are aware, it is the only available first-principles contact model. The model was applied in Ref. [33] to the contact between a tungsten AFM tip and graphene on an iridium substrate. A square-root dependence of the real contact area on load was found, i.e., $A(L) \propto L^{1/2}$. That result, however, was based on only a few data, motivating us to revisit the question of the load-dependent contact area in this system. To that end, we generate more data to better sample A as a function of L, and tried to refine the method for analyzing $A(L)$, but otherwise closely followed Ref. [33].

This thesis is structured as follows: In Chap. 2 we review some underlying theoretical concepts. Chap. 3 details the model and computational methods used. Chap. 4 summarizes the original result for $A(L)$ from Ref. [33]. Our extension of that work is found in Chap. 5, before we present our conclusions in Chap. 6.

2 Background

2.1 Macroscopic contact models

In this section we give an overview of some macroscopic contact models popular in the interpretation of AFM experiments, loosely based on Sec. 3.1 of Ref. [9]. For the most part, we restrict ourselves to stating the basic assumptions of each model and to its prediction for the load-dependent contact area between a sphere and a plane, as the model of an AFM-setup.

2.1.1 Hertz theory of nonadhesive contact

Modern contact mechanics was originated by Heinrich Hertz who was the first to develop a full-fledged theory of contact between nonadhesive bodies [35]. A more recent textbook treatment can be found in [1], which we will also partly follow here. Development of the theory by Hertz was originally motivated by a specific problem from his work. He was studying the interference patterns produced by the gap between glass lenses (*Newton's interference fringes*) and wanted to understand how elastic deformations resulting from contact pressure between the lenses might influence the patterns. Hertzian contact theory is not just of historical interest. It remains relevant and popular today, due to the relative simplicity of the relationships it predicts, paired with accuracy that is nonetheless often acceptable. We will therefore devote some space to a discussion of it.

Hertz adopted a description of the surface profiles of the two bodies in their undeformed state in the form of paraboloids. If we choose the origin O of our Cartesian coordinate system $Oxyz$ as the point at which the two bodies only just touch as they are brought in contact, but are not deformed yet, and define the Oxy plane as the two bodies' common tangent plane at that point, we can write the surface profiles in a vicinity of the point of contact as

$$z_1 = A_1x^2 + B_1y^2 + C_1xy, \quad z_2 = A_2x^2 + B_2y^2 + C_2xy\,. \tag{2.1}$$

The real profiles must be sufficiently smooth and symmetrical in the vicinity of the contact region for such a representation to be admissible.

Each of the two paraboloidal surface profiles is characterized by two principal radii of curvature (in terms of which the coefficients in Eq. 2.1 may be restated). Shapes that can be approximated by this description notably include spheres (where both radii of curvature are finite and equal) as well as cylinders (by letting one radius of curvature go to infinity) and planes (by letting both radii of curvature go to infinity). In addition to the radii of curvature, which describe the bodies' geometries, each body is characterized by two further parameters related to its mechanical properties. These are Young's modulus E and Poisson's ratio ν.

Hertz assumed that contact of two bodies with profiles as described above would, in the general case, give rise to contact regions bounded by elliptical contours. This is not self-evident from the outset but can be shown to be justified. On the other hand, if both bodies are solids of revolution (i.e., both have two identical radii of curvature), it is easy to conclude from symmetry arguments that the contact region will be bounded by a circle. We will denote the radius of this circle as a and refer to it as the *contact radius*.

With these preliminaries out of the way, we may now state the assumptions employed in Hertz theory to solve the actual contact problem.

1. The surfaces are microscopically smooth.
   Intuitively speaking, this is to say that no matter with how much magnification one looks at the surfaces, there will never be any microscopic irregularity detected, recall Eq. 2.1.

2. The surfaces are continuous and non-conforming.
   Non-conforming means that they initially touch only in a single point or along a line at most, but not over an extended area, and that the contact area still remains small compared to the surfaces' radii of curvature as a load is applied.

3. Strains are small and do not exceed the elastic limit.
   This allows the linear theory of elasticity to be used, with all the obvious advantages this entails.

4. For the purpose of calculating the local displacements relative to its undeformed state, each body can be treated as an elastic half-space loaded over an elliptical surface region.
   An elastic half-space is a region of space bounded by a plane and extending to infinity to one side of that plane. For this approximation to be valid, the contact region must be small compared to the overall size of the two bodies as well as compared to their surfaces' radii of curvature. The first condition justifies the neglect of boundary effects due to the bodies' finite size which the half-space approximation implies. The second condition ensures that the surfaces outside the contact region are sufficiently flat to be approximated as planar.

5. The surfaces are frictionless.
   Frictionless in this context means that no tangential forces are transmitted through the region of contact. Given the other assumptions already made (half-space approximation, linear elasticity) tangential forces are understood to be only those acting in the x and y directions, even though strictly speaking they will also have a small z component due to the generally curved contact areas.

We will now go straight to the results for our case of interest, which is the contact between a sphere of radius R and a plane. Hertz theory predicts that the contact radius a varies with the applied load L as

$$a_{\text{Hertz}}(L) = \left(\frac{RL}{K}\right)^{1/3}, \quad \text{with } K = \frac{4}{3}\left(\frac{1-\nu_1^2}{E_1} + \frac{1-\nu_2^2}{E_2}\right)^{-1}, \tag{2.2}$$

where the indices 1 and 2 label the two bodies. The mutual approach δ of distant points within the two bodies is given by

$$\delta_{\text{Hertz}}(L) = \frac{a_{Hertz}^2}{R} = \left(\frac{L^2}{RK^2}\right)^{1/3}. \tag{2.3}$$

In case when one body is rigid, δ can be understood as the indentation depth of the other one. The definition of these quantities and the deformation resulting from loading are shown schematically in Fig. 2.1, for the simple case of a rigid sphere.

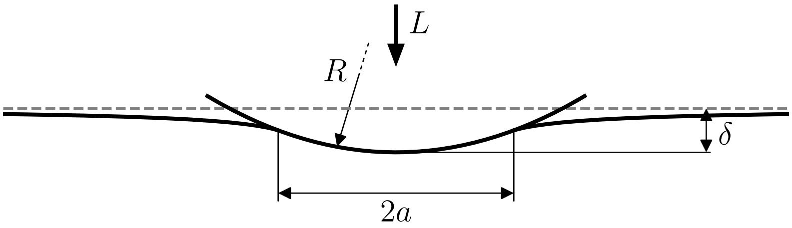

Fig. 2.1: Deformation of an elastic half-space upon indentation by a rigid sphere of radius R (approximated as a paraboloid).

To obtain the actual contact *area*, not just the contact radius, it is necessary to take into account the exact profile of the surfaces in the contact region. Although this profile will in general not be planar, the contact area A is commonly approximated as

$$A_{\text{Hertz}} \approx \pi \cdot (a_{\text{Hertz}})^2 \propto L^{2/3}. \tag{2.4}$$

Within the assumptions made already in Hertz theory, this is a justifiable approach. This will also remain true for the models going beyond Hertz theory discussed in the following sections.

2.1.2 Adhesive contacts

One of the most notable features of real contacts not included in Hertz theory is the adhesion. On the macroscale, adhesion is indeed often negligible. In microscopic contacts, however, it can be critically important. This is due to the different scaling behavior of surface area and bulk volume as a function of object size, which causes surface forces to become relatively more important the smaller the length scale.

A model for adhesive contact of elastic bodies was published in 1971 by Johnson, Kendall, and Roberts [36], known as the JKR model. It assumes that the adhesive interactions are infinitely short range. That means, they cause a lowering of the energy of the system only if two surfaces are in immediate contact, but there is no energy contribution from surfaces at any non-zero separation. The model's prediction for the load-dependent contact radius between a sphere of radius R and a plane is

$$a_{\mathrm{JKR}}(L) = \left(\frac{R}{K} \left[L + 3\pi\gamma R + \sqrt{6\pi\gamma R L + (3\pi\gamma R)^2} \right] \right)^{1/3} , \tag{2.5}$$

with K as in Eq. 2.2. The quantity γ is called the work of adhesion. It is equal to the work per unit area necessary to separate two surfaces to infinity, and is therefore a measure of the strength of the adhesive interactions.

In contrast to Hertz theory, the contact radius at zero load remains finite,

$$a_{0(\mathrm{JKR})} = \left(\frac{6\pi\gamma R^2}{K} \right)^{1/3} . \tag{2.6}$$

and a negative (i.e., tensile) load

$$L_{\mathrm{c(JKR)}} = -\frac{3}{2}\pi\gamma R \tag{2.7}$$

must be applied to separate the bodies, often called the *critical load* or the *pull-off force*. These are both consequences of the presence of adhesion.

In fact, the situation is a bit more complicated. The relation between a and L in the JKR model actually consists of two branches, and Eq. 2.5 describes only one of them (the upper branch in Fig. 2.2). The lower branch differs by the sign in front of the square-root term. The two branches meet in the point where $L = L_{\mathrm{c(JKR)}}$ (point I. in Fig. 2.2). In an experiment where one controls the applied load, the surfaces will spontaneously separate at the pull-off force, and points along the lower branch do not represent stable configurations. They are therefore inaccessible in such a 'load-control' setup, and we will accordingly call the lower branch the *unstable load region*. AFM nanofriction experiments with tips attached to a flexible cantilever fall into this 'load-control' category, meaning that the upper branch Eq. 2.5 describes the experimentally most relevant case. If, on the other hand, the displacement rather than the load is controlled, part of the unstable load branch is accessible, but there is a point at which the surfaces will separate spontaneously even in such a 'displacement-control' setup (point II. in Fig. 2.2) [37]. Qualitatively similar behavior is also seen in other adhesive contact models.

Not long after the JKR model, another model was presented by Derjaguin, Muller, and Toporov [38], known as the DMT model. They took a different approach by assuming that there is a long-range attractive interaction acting at all separations, and that the description of the elastic deformations by a Hertzian profile remains valid even in the presence of this interaction. The model's prediction for the size and load dependence of the contact radius is

$$a_{\mathrm{DMT}}(L) = \left(\frac{R}{K} \left[L + 2\pi\gamma R \right] \right)^{1/3} , \tag{2.8}$$

which is similar to the Hertz result Eq. 2.2, except an offset along the load axis. This load offset corresponds to the pull-off force, for which DMT theory predicts

$$L_{\mathrm{c(DMT)}} = -2\pi\gamma R \, . \tag{2.9}$$

Unlike in the JKR model, the contact area in the DMT model goes to zero continuously as the pull-of force is approached, and there is no unstable load branch (see Fig. 2.2). At $L = 0$, the contact radius takes the value

$$a_{0\mathrm{(DMT)}} = \left(\frac{2\pi\gamma R^2}{K} \right)^{1/3} . \tag{2.10}$$

The apparent incompatibility of the JKR and DMT models generated a fair amount of debate. This went on until the realization by Tabor [40] that the two models in fact represent completely opposite limiting cases of adhesive elastic contacts, and that they are both correct in their respective regime of validity. The JKR model applies if the elastic deformations caused by the adhesive interactions are large compared to the range of the interactions. This is the case for soft materials, large tip radii, and strong, short-range adhesion forces. If, on the other hand, elastic deformations due to adhesion are small compared to the range of the interactions producing them, the DMT model is appropriate. This occurs for hard materials, small tip radii and weak, long-range interaction forces. To distinguish between the two limits, a dimensionless parameter, known as the *Tabor parameter* [40, 41], can be convenient. It is given by

$$\mu_T = \left(\frac{16 R \gamma^2}{9 K^2 z_0^3} \right)^{1/3} , \tag{2.11}$$

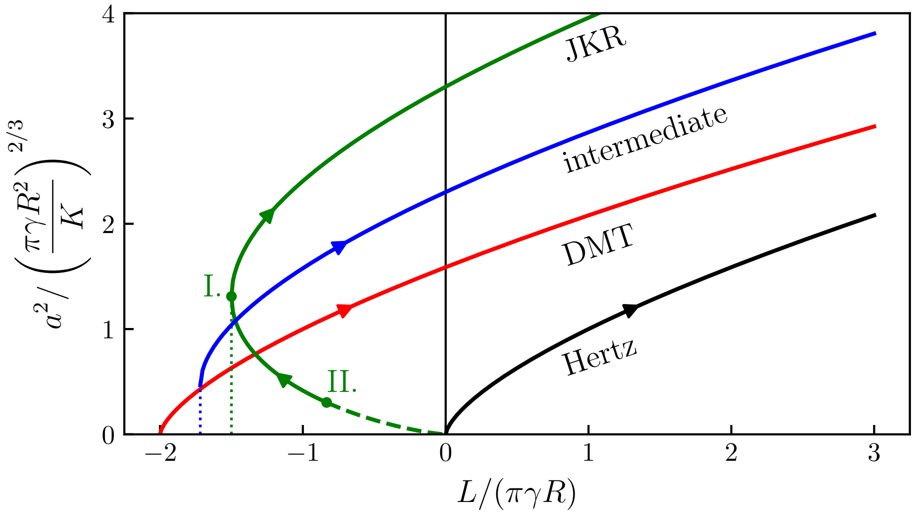

Fig. 2.2: Square of contact radius as a function of load in various models. Plotted in Maugis' dimensionless units [39]. Arrows on the curves indicate increasing approach between the two bodies. For the intermediate case, only the stable load branch is shown, which was drawn using Eq. 2.13.

with z_0 being the equilibrium separation of the surfaces. As long as z_0 is the only intrinsic length scale of the interaction potential, it can be seen as a measure of the range of the interaction. The Tabor parameter expresses the ratio between elastic deformations induced by adhesion alone (not due to an applied load) and the range of the adhesive interaction as measured by z_0. JKR theory is appropriate in the limit of large μ_T, DMT theory at small μ_T.

Understanding of the JKR-DMT transition was deepened by Maugis, who worked out an analytic solution of the contact behavior in the intermediate regime. To do so, he assumed a constant adhesive stress σ_0 acting between the surfaces up to a separation δ_t, and no interaction at larger separations. Such a type of interaction is known as a Dugdale potential and Maugis' model is therefore referred to as the *Maugis-Dugdale* model. The work of adhesion in this model is simply given by $\gamma = \sigma_o \cdot \delta_t$. Maugis introduced a transition parameter

$$\lambda = 2\sigma_0 \left(\frac{R}{\pi\gamma K^2}\right)^{1/3} , \qquad (2.12)$$

which possesses a similar interpretation as μ_T. JKR theory is applicable when $\lambda > 5$, DMT theory is applicable when $\lambda < 0.1$, and values in between indicate the transition regime between the two. While Maugis' solution in the transition regime is mathematically exact, it is also rather unwieldy and notably does not come in the form of one single formula expressing a as a function of L. This limits its application in practice, where one typically measures the frictional force F_f (related to the area of contact, and thus to a, by Eq. 1.2) as a function of load, and wants to fit an analytic expression to these data.

This was remedied to some extent by Carpick, Ogletree, and Salmeron [42]. They proposed a formula for $a(L)$ that approximates (the stable load branch of) the Maugis-Dugdale solution in the intermediate regime with high accuracy, while being easier to use. This *generalized transition equation* is given by

$$a(L) = a_0 \left(\frac{\alpha + \sqrt{1 - L/L_c}}{1 + \alpha} \right)^{2/3} . \tag{2.13}$$

It uses three fit parameters, a_0, L_c and α. The parameter α governs the transition between JKR and DMT and can be mapped onto Maugis' λ. A value of $\alpha = 0 \iff \lambda = 0$ corresponds to the exact DMT limit, and $\alpha = 1 \iff \lambda = \infty$ to the exact JKR limit.

The Dugdale potential used in Maugis' analytic solution is of course still an idealization. But it turns out that the predicted contact behavior is relatively insensitive to the precise shape of the interaction potential [43]. This makes the Maugis-Dugdale model quite widely applicable despite its idealizations. Furthermore, more realistic interaction potentials can generally only be treated numerically.

2.1.3 Thin-Coating Contact Mechanics

The models covered so far all have in common that the contacting bodies are assumed homogeneous. In many applications, however, one or both contacting bodies are composed of multiple layers with different elastic properties. An example of such a layered composition is when one of the surfaces is covered by a thin coating. We will now briefly review one simple and easy-to-use theory for this case developed by Reedy [44], termed *Thin-Coating Contact Mechanics* (TCCM).

The model considers the contact between a rigid spherical indenter and a thin, linear elastic coating bonded to a rigid substrate. The coating is characterized by its thickness h, Young's modulus E, and Poisson's ratio ν. The spherical indenter has the radius R. The model assumes that the coating thickness and the contact radius are much smaller than the indenter radius ($h/R,\ a/R \ll 1$), and the contact radius much larger than the coating thickness ($a/h \gg 1$). More compactly, $h \ll a \ll R$. Importantly, the model is not valid for incompressible coatings ($\nu \approx 0.5$), which require a separate analysis.

Reedy expressed his results using dimensionless variables. In a notation slightly adapted for consistency with the previous sections, these quantities are given by

$$\bar{a} = \frac{a}{\sqrt{Rh}}, \; \bar{h} = \frac{h}{\sqrt{Rh}}, \; \bar{\gamma} = \frac{\gamma}{E_u h}, \; \bar{L} = \frac{L}{E_u R h}\,, \tag{2.14}$$

with the so-called uniaxial strain modulus

$$E_u = \frac{1-\nu}{(1+\nu)(1-2\nu)} E\,. \tag{2.15}$$

In the absence of adhesion, TCCM predicts a square-root behavior of the contact area as a function of applied load,

$$(\bar{a}_{\text{TC-noadh}})^2 = \left(\frac{4}{\pi}\bar{L}\right)^{1/2}\,, \tag{2.16}$$

in notable contrast to the 2/3-power dependence in Hertz theory. In addition to the adhesionless case, Reedy also worked out two different versions of the thin-coating theory that include adhesion. The first one assumes DMT-like adhesive behavior, which leads to

$$(\bar{a}_{\text{TC-DMT}})^2 = \left(\frac{4}{\pi}[\bar{L} + 2\pi\bar{\gamma}]\right)^{1/2}\,. \tag{2.17}$$

The second one assumes JKR-like adhesive behavior, resulting in

$$(\bar{a}_{\text{TC-JKR}})^2 = (8\bar{\gamma})^{1/2} \pm \left(\frac{4}{\pi}[\bar{L} + 2\pi\bar{\gamma}]\right)^{1/2}\,. \tag{2.18}$$

Like the standard JKR model, this also has two branches.

Strictly speaking, the formulas of TCCM only hold for h/R and a/R vanishingly small. However, Reedy proposed an extension of the nonadhesive result Eq. 2.16 even to cases where this is not strictly satisfied by assuming a general power-law

$$\bar{a}^2 = \left(\frac{4}{\pi}\right)^{1/2} c \cdot \bar{L}^d\,, \tag{2.19}$$

with the fitting parameters c and d that are expected to be functions of ν and h/R. To assess this behavior, Reedy performed finite-element method (FEM) simulations for ν ranging from 0.00–0.45 and h/R from 0.01–0.10. For each parameter combination the indentation δ of the coating was limited to $\delta/h < 0.2$ (considered a plausible upper limit to linear elastic behavior). Some deviations of the FEM results from Eq. 2.16 were observed, but agreement was found to be excellent across all parameter values considered when fitting the general power-law Eq. 2.19 to the data.

2.2 Density-Functional Theory

If one wants to simulate the behavior of atoms, molecules or solids without relying on empiricism, one needs to solve the many-body Schrödinger equation (SE) $\hat{H}\left|\Psi\right\rangle = i\hbar\partial_t\left|\Psi\right\rangle$ (or its stationary version $\hat{H}\left|\Psi\right\rangle = E\left|\Psi\right\rangle$). In principle, this provides a complete description. In practice, however, an exact solution of the full many-body SE is hopelessly out of reach for all but the smallest systems. The problem lies in the immense complexity of the central mathematical object, the wave function Ψ. For N particles in 3 dimensions, it is a function of $3N$ coordinates (spin not considered), meaning that the memory requirements scale exponentially with the number of particles.

To bring down the computational cost to a feasible level, while retaining acceptable accuracy, many clever approximations have been developed. Of outstanding importance among them is *density-functional theory* (DFT), which manages to avoid the scaling problem by working with the one-particle density rather than the wave function. The benefit of this is clear, as the one-particle density is always a function of just 3 coordinates, regardless of the number of particles.

In this section, we will give a brief overview of DFT, based on [45, 46].

2.2.1 Hamiltonian and Born-Oppenheimer Approximation

We first introduce the general many-body Hamiltonian and the Born-Oppenheimer or 'adiabatic' approximation [47], which form the starting point for our discussion of DFT. These concepts, however, are by no means specific to DFT.

Without external fields, the non-relativistic many-body Hamiltonian reads

$$\hat{H} = \underbrace{\sum_{I=1}^{N_n} \frac{\hat{\mathbf{P}}_I^2}{2M_I}}_{\hat{T}_n} + \underbrace{\sum_{i=1}^{N_e} \frac{\hat{\mathbf{p}}_i^2}{2m}}_{\hat{T}_e} + \underbrace{\sum_{I<J} \frac{Z_I Z_J e^2}{|\mathbf{R}_I - \mathbf{R}_J|}}_{V_{nn}} + \underbrace{\sum_{i<j} \frac{e^2}{|\mathbf{r}_i - \mathbf{r}_j|}}_{V_{ee}} - \underbrace{\sum_{I,j} \frac{Z_I e^2}{|\mathbf{R}_I - \mathbf{r}_j|}}_{V_{ne}}, \tag{2.20}$$

where upper-case indices iterate over nuclei, lower-case ones over electrons. N_n and N_e are the numbers of nuclei and electrons, respectively. $\mathbf{P}_I$, $\mathbf{R}_I$ and M_I denote the nuclear momenta, positions and masses, $\mathbf{p}_i$, $\mathbf{r}_i$ and m are those of the electrons. The Z_I are the atomic numbers of the nuclei, and e is the elementary charge.

The Schrödinger equation of this Hamiltonian, in position space, reads

$$\left[\hat{T}_n + \hat{T}_e + V_{nn} + V_{ee} + V_{ne}\right]\Psi\big(\{\mathbf{r}_i, \mathbf{R}_I\}\big) = E_{tot}\Psi\big(\{\mathbf{r}_i, \mathbf{R}_I\}\big)\,. \tag{2.21}$$

To simplify this equation, the Born-Oppenheimer approximation exploits the different time scales of electronic and ionic motion, due to the electrons' much lower mass, in order to decouple them. First, we write $H_e = T_e + V_{ee} + V_{ne}$ and suppose that the eigenfunctions $\phi_\alpha\big(\{\mathbf{r}_i, \mathbf{R}_I\}\big)$ of H_e, with corresponding eigenenergies $E_{e,\alpha}\big(\{\mathbf{R}_I\}\big)$, are known:

$$\Big[\hat{T}_e + V_{ee} + V_{ne}\Big]\phi_\alpha\big(\{\mathbf{r}_i, \mathbf{R}_I\}\big) = E_{e,\alpha}\big(\{\mathbf{R}_I\}\big)\,\phi_\alpha\big(\{\mathbf{r}_i, \mathbf{R}_I\}\big)\,. \tag{2.22}$$

Note that in this equation the dependence on the nuclear positions $\mathbf{R}_I$ is only of a parametric kind, since H_e contains no derivative w.r.t. them. Since the $\phi_\alpha\big(\{\mathbf{r}_i, \mathbf{R}_I\}\big)$ form a complete basis set, we can, for any fixed set $\{\mathbf{R}_I\}$ of nuclear positions, expand a solution $\Psi\big(\{\mathbf{r}_i, \mathbf{R}_I\}\big)$ of the full Schrödinger equation Eq. 2.21 as:

$$\Psi\big(\{\mathbf{r}_i, \mathbf{R}_I\}\big) = \sum_\alpha \chi_\alpha\big(\{\mathbf{R}_I\}\big)\phi_\alpha\big(\{\mathbf{r}_i, \mathbf{R}_I\}\big)\,. \tag{2.23}$$

This ansatz, plugged into the full Schrödinger equation Eq. 2.21, together with neglecting some terms proportional to powers of m/M_I, finally leads to

$$\Big[\hat{T}_n + V_{nn} + E_{e,\alpha}\big(\{\mathbf{R}_I\}\big)\Big]\chi_\alpha\big(\{\mathbf{R}_I\}\big) = E_{tot}\,\chi_\alpha\big(\{\mathbf{R}_I\}\big)\,. \tag{2.24}$$

The interpretation of Eq. 2.22 is that the electrons move in the potential generated by the nuclei, and that is perceived by them as static. Eq. 2.24 expresses that the nuclei move on the potential-energy surface generated by the electronic eigenenergies (through their parametric dependence on $\{\mathbf{R}_I\}$), and that the electron states adapt to the nuclear motion adiabatically (i.e., the electrons do not undergo transitions).

As a further approximation, we shall treat only the electrons quantum mechanically, by means of Eq. 2.22, and describe the nuclei by classical equations of motion

$$M_I\ddot{\mathbf{R}}_I = -\frac{\partial}{\partial \mathbf{R}_I}E_{tot}\big(\{\mathbf{R}_I\}\big) = -\frac{\partial}{\partial \mathbf{R}_I}\Big[V_{nn}\big(\{\mathbf{R}_I\}\big) + E_{e,\alpha}\big(\{\mathbf{R}_I\}\big)\Big]\,. \tag{2.25}$$

2.2.2 Hohenberg-Kohn Theorems

Having separated electronic and nuclear motion by means of the Born-Oppenheimer approximation, we are now only concerned with the electronic Schrödinger equation Eq. 2.24. To reduce clutter, we drop all subscripts distinguishing nuclei and electrons, as well as references to parametric dependences on nuclei positions, and write $\hat{T}_{ee} \equiv \hat{T}$, $V_{ee} \equiv U$, and $V_{ne} \equiv V = \sum_{i=1}^{N_e} v(\mathbf{r}_i)$. Any additional external potential the electrons may be subject to other than that generated by the fixed nuclei is also put into $v(\mathbf{r}_i)$. Next, we define the one-particle density of the electrons

$$n(\mathbf{r}) = \langle \phi | \sum_{i=1}^{N_e} \delta(\mathbf{r} - \mathbf{r}_i) \, |\phi\rangle \ . \tag{2.26}$$

With this, we are ready to review the theorems by P. Hohenberg and W. Kohn [48] (HK) that form the basis of DFT:

Theorem 1 *The external potential $v(\mathbf{r})$ is, up to an additive constant, a unique functional of the ground-state density $n_0(\mathbf{r})$.*

This statement is proved by contradiction. Assume there exist two different external potentials $v^{(1)}(\mathbf{r})$ and $v^{(2)}(\mathbf{r})$ that both give rise to the same ground-state density $n_0(\mathbf{r})$. Apart from the external potential, the Hamiltonians of the two systems are the same, since $\hat{T}$ and U depend only on the number of electrons N_e (which for a given density $n_0(\mathbf{r})$ is fixed). They read

$$\begin{aligned} \hat{H}^{(1)} &= \hat{T} + U + V^{(1)}, \quad \text{with} \quad V^{(1)} = \sum_{i=1}^{N_e} v^{(1)}(\mathbf{r}_i) \\ \hat{H}^{(2)} &= \hat{T} + U + V^{(2)}, \quad \text{with} \quad V^{(2)} = \sum_{i=1}^{N_e} v^{(2)}(\mathbf{r}_i) \, . \end{aligned} \tag{2.27}$$

Except for the trivial case $v(\mathbf{r})^{(1)} - v(\mathbf{r})^{(2)} = \text{const.}$, the ground states $\phi_0^{(1)}$ and $\phi_0^{(2)}$ of $\hat{H}^{(1)}$ and $\hat{H}^{(2)}$ cannot be the same. This allows us to compute

$$\begin{aligned} E_0^{(1)} = \langle \phi_0^{(1)} | \, \hat{H}^{(1)} \, |\phi_0^{(1)} \rangle < \langle \phi_0^{(2)} | \, \hat{H}^{(1)} \, |\phi_0^{(2)} \rangle & \\ = \langle \phi_0^{(2)} | \, \hat{H}^{(2)} \, |\phi_0^{(2)} \rangle + \langle \phi_0^{(2)} | \, V^{(1)} - V^{(2)} \, |\phi_0^{(2)} \rangle & \\ = E_0^{(2)} + \int n_0(\mathbf{r}) \left(v^{(1)}(\mathbf{r}) - v^{(2)}(\mathbf{r}) \right) \mathrm{d}^3 r \, , & \end{aligned} \tag{2.28}$$

where the inequality is because the expectation value of $\hat{H}^{(1)}$ is minimal when evaluated with its correct ground state, by the variational principle. The same calculation with the roles of (1) and (2) reversed gives

$$E_0^{(2)} < E_0^{(1)} + \int n_0(\mathbf{r}) \left(v^{(2)}(\mathbf{r}) - v^{(1)}(\mathbf{r}) \right) \mathrm{d}^3 r \, . \tag{2.29}$$

Addition of Eq. 2.28 and Eq. 2.29 leads to a contradiction,

$$E_0^{(1)} + E_0^{(2)} < E_0^{(2)} + E_0^{(1)} \, . \tag{2.30}$$

The starting assumption of two different external potentials that produce the same ground-state density must therefore have been wrong.

$\hat{T}$ and U follow straightforwardly from $n_0(\mathbf{r})$ via $N_e = \int n_0(\mathbf{r})\,\mathrm{d}^3 r$, and we have just seen that $v(\mathbf{r})$, too, is uniquely determined by $n_0(\mathbf{r})$. The Hamiltonian as a whole is therefore uniquely determined by $n_0(\mathbf{r})$. Consequently, the ground state $\phi_0[n_0]$ is also a unique functional of n_0 (assuming no degeneracy), as is the ground-state energy $E_0[n_0]$. More than that, $n_0(\mathbf{r})$ strictly speaking determines even the entire spectrum through its fixing of $\hat{H}$.

We now introduce the density functional of the energy

$$E[n] \coloneqq \min_{\phi\to n} \langle\phi|\,\hat{H}\,|\phi\rangle = \min_{\phi\to n} \langle\phi|\,\hat{T} + U + V\,|\phi\rangle \equiv T[n] + U[n] + V[n]\,, \tag{2.31}$$

where the minimization condition means the minimum out of all states ϕ that produce the given density n. For this functional, it holds that:

Theorem 2 *The functional $E[n]$ assumes its minimum value at the correct ground-state density n_0, for fixed particle number N_e.*

This is a consequence of the first HK Theorem in combination with the general variational principle of quantum mechanics.

2.2.3 Kohn-Sham Equations

By virtue of the HK theorems, the problem of finding the ground-state density and energy becomes that of minimizing the density functional $E[n]$ given by Eq. 2.31—in principle a much more manageable task than searching for the full wave function. However, in practice one is hindered by the lack of an explicit expression for $E[n]$. The HK theorems only establish the existence and uniqueness of $E[n]$ but do not declare how it looks like.

Only the external potential contribution $V[n] = \int n(\mathbf{r})v(\mathbf{r})\,\mathrm{d}^3 r$ is known explicitly in terms of the density. A natural, but only approximate, ansatz for expressing $U[n]$ in terms of $n(\mathbf{r})$ is the Hartree [49] energy

$$U[n] \approx \frac{e^2}{2}\int\!\!\int \frac{n(\mathbf{r})n(\mathbf{r}')}{|\mathbf{r}-\mathbf{r}'|}\,\mathrm{d}^3 r\,\mathrm{d}^3 r' \equiv U_H[n]\,. \tag{2.32}$$

Expressing the remaining part, the kinetic energy $T[n]$, in terms of the density is particularly problematic.

However, explicit minimization of $E[n]$ over $n(\mathbf{r})$ is not the only possible approach. There is another way, due to W. Kohn and L. J. Sham [50], that improves the treatment of the kinetic energy by reintroducing wave functions. Kohn and Sham considered an auxiliary system of N_e non-interacting electrons moving in a fictitious single-particle potential $v_{\text{eff}}(\mathbf{r})$ that reproduces the density of the real interacting system. The wave function of such a non-interacting system can be written as a Slater determinant composed of N_e single-particle orbitals φ_i, and the density reads simply

$$n(\mathbf{r}) = \sum_{i=1}^{N_e} |\varphi_i(\mathbf{r})|^2 \,. \tag{2.33}$$

The kinetic energy of the non-interacting system (subscript s for 'single-particle') can be expressed as

$$T_s[\{\varphi_i\}] = -\frac{\hbar^2}{2m} \sum_{i=1}^{N_e} \int \varphi_i^*(\mathbf{r}) \nabla^2 \varphi_i(\mathbf{r}) \, \mathrm{d}^3\, r \,. \tag{2.34}$$

Based on the kinetic energy of the non-interacting system, the ansatz

$$E[\{\varphi_i\}] = T_s[\{\varphi_i\}] + U_H[n] + V[n] + E_{xc}[n] \tag{2.35}$$

is made for the energy of the real interacting system. The so-called exchange-correlation term $E_{xc}[n]$ summarizes all corrections due to the difference between the single-particle kinetic energy $T_s[\{\varphi_i\}]$ and $T[n]$ of the interacting system, as well as between the Hartree energy $U_H[n]$ and the exact $U[n]$. It is customarily further decomposed into $E_{xc}[N] = E_x[n] + E_c[n]$, where the exchange part $E_x[n]$ is due to the Pauli exclusion principle and the correlation part $E_c[n]$ is due to the tendency of electrons to avoid each other because of Coulomb repulsion.

Variation of Eq. 2.35 w.r.t. the orbitals φ_i^*, under the normalization constraint $\int \varphi_i^* \varphi_i \, \mathrm{d}^3\, r = 1 \; \forall i$, yields the Kohn-Sham equations

$$\Bigg(-\frac{\hbar^2}{2m} \nabla^2 + \underbrace{v(\mathbf{r}) + \int \frac{e^2 n(\mathbf{r}')}{|\mathbf{r} - \mathbf{r}'|} \, \mathrm{d}^3\, r' + \frac{\delta E_{xc}[n]}{\delta n(\mathbf{r})}}_{v_{\text{eff}}(\mathbf{r})} \Bigg) \varphi_i(\mathbf{r}) = \epsilon_i \varphi_i(\mathbf{r}) \,. \tag{2.36}$$

The Kohn-Sham equations form the basis of most modern DFT applications. Formally, they look like N_e one-particle Schrödinger equations for electrons in an effective external potential $v_{\text{eff}}(\mathbf{r})$. However, since $v_{\text{eff}}(\mathbf{r})$ depends itself on the density and thus on the orbitals, these equations are nonlinear. To solve them, one typically applies an iterative self-consistency procedure:

1. Start with a guess for the density $n(\mathbf{r})$.

2. From the density, construct $v_{\text{eff}}(\mathbf{r})$.
3. Plug $v_{\text{eff}}(\mathbf{r})$ into the Kohn-Sham equations and solve for the orbitals φ_i.
4. Recompute the density from the resulting orbitals, by means of Eq. 2.33.
5. If the change in the energy $E[n]$ compared to the previous iteration is smaller than a set threshold, halt. Otherwise, repeat from 2. with the new density.

While we have not considered it in this introduction, it is also possible to extend this formalism to include electron spin.

2.2.4 Exchange-correlation functionals

The Kohn-Sham equations are formally exact since, by definition, all many-body effects not accounted for by $T_s[\{\varphi_i\}]$ and $U_H[n]$ are contained in the exchange-correlation energy $E_{xc}[n]$. However, in practice, $E_{xc}[n]$ is unknown and one must rely on approximations for it. The accuracy of DFT hinges thus on the quality of these approximations. Over time, a plethora of different approximations with varying degrees of sophistication have been developed. The choice of functional generally depends on the problem at hand.

The simplest approximations for $E_{xc}[n]$ are based on the homogeneous electron gas. Starting from expressions $\varepsilon_{xc}^{\text{hom}}(n^{\text{hom}})$ for the per-volume exchange-correlation energy derived initially for the homogeneous electron gas, one simply replaces the constant density n^{hom} in these expressions with a spatially varying one:

$$E_{xc}[n] \approx \int \varepsilon_{xc}^{\text{hom}}(n(\mathbf{r}))\, \mathrm{d}^3 r\,. \tag{2.37}$$

This approximation can be justified for slowly-varying densities, but gives surprisingly good results even in situations where this is not the case. Since the resulting exchange-correlation potential depends only on the value of the density at the position $\mathbf{r}$, this kind of approximation is known as a *local-density approximation* (LDA).

One may imagine that the exchange-correlation energy can be more accurately captured by incorporating not just the local value $n(\mathbf{r})$ of the density, but also its slope $\nabla n(\mathbf{r})$. The resulting *generalized-gradient approximation* (GGA) has the general form

$$E_{xc}^{\text{GGA}}[n] = \int \varepsilon_{xc}(n(\mathbf{r}), \nabla n(\mathbf{r}))\, \mathrm{d}^3 r\,. \tag{2.38}$$

Further extensions include the meta-GGA functionals, where the Kohn-Sham kinetic energy density $\tau(\mathbf{r}) = \hbar^2/(2m) \sum_{i=1}^{N_e} |\nabla\varphi_i|^2$ is added as another descriptor.

So-called hybrid functionals, combine exchange-correlation density functionals with a portion of exact Hartree-Fock exchange. Meta-GGAs and hybrid functionals are both examples of so-called orbital functionals, since they express E_{xc} not fully in terms of the density but also partly in terms of the Kohn-Sham orbitals φ_i.

To describe long-range van-der-Waals interactions, which are related to non-local correlations, methods are required that go beyond the (semi-)local approximations made in LDA and GGA. An overview can be found in [51]. One successful method that is convenient and not too costly is vdW-DF by Dion and co-workers [52]:

$$E_{xc}[n] \approx E_x^{\mathrm{GGA}}[n] + E_c^{\mathrm{LDA}}[n] + E_c^{\mathrm{nl}}[n] \,. \tag{2.39}$$

It uses a GGA functional for exchange, and decomposes the correlation part into a local contribution from LDA and a non-local contribution

$$E_c^{\mathrm{nl}}[n] = \frac{1}{2}\int\int n(\mathbf{r})\Phi(\mathbf{r},\mathbf{r}')n(\mathbf{r}')\,\mathrm{d}^3\,r\,\mathrm{d}^3\,r' \;, \tag{2.40}$$

with an interaction kernel $\Phi(\mathbf{r},\mathbf{r}')$. An important step in making vdW-DF practically useful was the development of an efficient algorithm [53] for the evaluation of the double integral in Eq. 2.40. In this thesis, the optB86b-vdW version of vdW-DF is used, which is obtained by setting the exchange term of Eq. 2.39 to the optB86b functional proposed for that purpose by Klimeš and co-workers [54].

2.2.5 Geometry optimization

DFT as presented so far provides the density and energy of the electronic ground state, for a given fixed configuration of nuclei. The resulting electronic ground-state energy $E_{e,0}(\{\mathbf{R}_I\})$ thus depends parametrically on the configuration $\{\mathbf{R}_I\}$ of nuclei. The total energy of a configuration,

$$E_{tot}(\{\mathbf{R}_I\}) = V_{nn}(\{\mathbf{R}_I\}) + E_{e,0}(\{\mathbf{R}_I\}) \,, \tag{2.41}$$

consists of the electronic contribution and the contribution V_{nn} from the nucleus-nucleus Coulomb interactions (see also Sec. 2.2.1). The equilibrium configuration of nuclei is the one that minimizes E_{tot}. The problem of finding this configuration is known as geometry optimization or relaxation[1]. Most minimization algorithms require the derivative of E_{tot} w.r.t. the $\mathbf{R}_I$. For implementation purposes, the computation of this derivative can be greatly facilitated by making use of the Hellmann-Feynman theorem [55].

---

[1] More generally, this may involve optimization also w.r.t. the size and shape of the simulation cell, not just the nuclei positions.

2.3 Quantum Theory of Atoms in Molecules

The *Quantum Theory of Atoms in Molecules* (QTAIM) by Richard Bader (see [56] for an overview, [34] for a comprehensive treatise) seeks to resolve a certain mismatch between the description of bound systems of atoms by traditional methods of chemistry and by quantum mechanics. The prevailing notion in chemistry, forming its operational basis, is that of individual atoms as building blocks of molecules and solids, linked together by chemical bonds. In this view, each individual atom possesses some characteristic and quantifiable properties. Quantum mechanics, on the other hand, treats the total system, with no such intrinsic notion of individual, delimitable atoms. If there is indeed some validity to the more local approach taken by chemistry, which is certainly suggested by its being quite successful, it stands to reason that a similar kind of local description is also contained within quantum mechanics. After all, its fundamental object, the wave function Ψ, provides the most complete information possible about a system.

QTAIM therefore asks about the possibility of formulating quantum mechanics not just for the total system, but open subsystems of it. The central result is that this can indeed be done, but only for subsystems that fulfill a certain boundary condition. This condition is a topological property of the electron density $n(\mathbf{r})$, namely that the subsystems must be bounded by zero flux surfaces of the gradient field of the electron density. Expressed mathematically, the subsystems are regions Ω in real space such that the gradient ∇n of the electron density is orthogonal to the surface normal vector $\vec{n}$ at all points $\mathbf{r}$ of the surface $S(\Omega)$ that bounds Ω,

$$\nabla n(\mathbf{r}) \cdot \vec{n}(\mathbf{r}) = 0 \quad \forall\, \mathbf{r} \in S(\Omega)\,. \tag{2.42}$$

This condition is rigorously derived from Schwinger's principle of stationary action [57], a variational principle giving rise to the equations of motion of quantum mechanics that is appropriately general to be extended to an open subsystem of the total system in a nonarbitrary fashion.

Space is thus partitioned into regions Ω according to Eq. 2.42. This partitioning is further shown to be unique and non-overlapping. Very often, each region defined this way contains a single nucleus [58]. The regions are therefore identified with the atoms, and referred to as *Bader atoms.*

A number of useful properties and applications follow from the result Eq. 2.42. An immediate consequence is that the individual Bader atoms make additive contributions to the total expectation value of an observable. This can be seen as recovering a central principle of chemistry on the basis of quantum mechanics. Another consequence is that versions of the Ehrenfest and virial theorems hold for the subsystems. Perhaps the most common and well-known application of QTAIM is Bader charge analysis, where the partitioning stipulated by Eq. 2.42 is used to divide charge densities between atoms, to study, e.g., charge redistribution in chemical reactions or dipole moments of individual atoms.

2.3.1 Molecular structure

Within the framework of QTAIM, Bader and coworkers also developed a theory of bonding and molecular structure based on topological properties of the electron density, which we will briefly discuss. To do so, we first need to introduce critical points of the charge density, and their classification. Critical points of the charge density are points where its gradient vanishes, $\nabla n(\mathbf{r}) = 0$. Different kinds of critical points are characterized and distinguished by a tuple (σ, λ), where σ indicates the rank of the Hessian matrix at the critical point, and λ is the sum of the signs of its eigenvalues (curvatures). At the positions of nuclei, maxima of $n(\mathbf{r})$, i.e. $(3, -3)$ critical points, are found. In the interatomic surfaces between some, but not all, Bader atoms bordering one another, $(3, -1)$ critical points are located. These constitute saddle points of $n(\mathbf{r})$, with a maximum along two spatial directions (tangential to the surface) and a minimum along a third direction (perpendicular to the surface). Two gradient paths (paths following the steepest ascent of $n(\mathbf{r})$) originate in such a critical point—one to either side of the surface—and terminate at the nuclei of the two Bader atoms.

Such a line formed by gradient paths, running from nucleus to nucleus and crossing the interatomic surface at a $(3, -1)$ critical point, is called an *atomic interaction line*. It possesses the important property that $n(\mathbf{r})$ is maximal along this path compared to any neighboring path linking the same pair of nuclei. Charge is therefore accumulated along this line, which is a necessary and, under certain additional assumptions, sufficient condition that there is a force binding the two nuclei together. In that case, the atomic interaction line is called a *bond path*. Note, however, that a bond path itself is not the same thing as a 'bond' but rather is a feature of the electron density indicating that two atoms are bonded to each other.

The network of all atomic interaction lines between the atoms of a molecule is referred to as the *molecular graph*. Its topology is found to match the assignment of chemical bonds by traditional chemistry. QTAIM regards two different configurations of nuclear positions as the same chemical structure if their molecular graphs are topologically equivalent. Conversely, the transition between two distinct chemical structures is marked by a change in the topology of the molecular graph. This further leads to the notion of stability in QTAIM as that of chemical structures which do not change their molecular graph as they undergo vibrations.

3 Model and Computational Methods

The fundamental model and methods used in this thesis are very closely based on the previous study by M. Wolloch *et al.* [33]. This includes using the model introduced therein for the *ab-initio* definition and calculation of contact areas on the atomic scale, and applying it to the same AFM model system as in that study. We also did not make any significant changes to the simulation parameters from back then, which had themselves been based partly on earlier studies by A. Garhofer [59], unless explicitly stated. We worked starting from input parameter files and atomic structures supplied by M. Wolloch.

Where we extend, and depart from, the previous work is mostly by trying to deepen and refine the analysis of the load dependence of the real contact area (which, too, was already touched upon in the original study, but on the basis of only few data, see Chap. 4). Our changes and extensions thus mostly do not concern the fundamental model and methods. We will report on them when we discuss our findings in Chap. 5, rather than in this chapter. From the outset, it has always been the aim of this thesis to refine the analysis of the load-dependence of the real contact area, building on the previous work by Wolloch *et al.*, without overly spending time and effort on redeveloping the fundamental method and simulation parameters. After all, this has already been done.

3.1 General

The supercell used to study the system is depicted in Fig. 3.1. The dimensions along the directions a, b and c are 24.61 Å, 24.61 Å and 26.53 Å, respectively. In the lower portion of the cell, there are four 9×9 layers of iridium (111). These form the substrate on which a 10×10 graphene layer is adsorbed, giving rise to a moiré structure. The simulation cell further contains a tungsten AFM tip, modeled as a pyramid-like structure of 10 atoms arranged in 3 layers. Its topmost layer (the 'tip base') has five atoms, the middle layer has four atoms, and the bottommost layer (the 'tip apex') is made up of just a single atom. The tip employed is therefore of the 'atomically sharp' kind. The total number of atoms in the supercell for the setup described is 534: 324 iridium, 200 carbon, and 10 tungsten atoms.

The lateral placement of the tip is such that the tip apex atom is above a carbon atom in a so-called top-hcp region of the graphene moiré structure. A top-hcp region is one where the carbon atoms are placed directly above the atoms of the first ('top site') and the second layer ('hcp site') of the substrate [60]. This is the only contact site between tip and surface that was considered in this work. Conceivably, contact behavior may depend on the contact site (i.e., the lateral tip position). For comparison with experimental friction forces, which are typically obtained as averages over an extended sliding path, it might be advisable to calculate contact areas by our method for different contact sites and finally to take an average. However, this was infeasible in the available time, given the sizeable computational cost of treating even a single contact site.

All simulations were performed by means of non-spin-polarized density-functional theory (DFT), using the plane-wave-based implementation provided by the Vienna *Ab-Initio* Simulation Package (VASP) [61–64], version 5.4.4. We used the projector augmented-wave (PAW) method [65, 66] in our calculations. Van-der-Waals (vdW) interactions, considered relevant in the system under study, were incorporated by choosing the optB86b-vdW functional [52–54]. The lattice constants of graphene and iridium[2] calculated with this functional are $a_{\mathrm{Gr}} = 2.465\,\text{Å}$ and $a_{\mathrm{Ir}} = 2.735\,\text{Å}$, in good agreement with experimental values of 2.46 Å and 2.71 Å (values reported from [59], we did not re-perform this calculation). The Brillouin zone was sampled on a Γ-centered $3 \times 3 \times 1$ k grid, with a smearing of 0.1 eV applied using the scheme of Methfessel and Paxton [67] to first order. Electronic energies were converged to 10^{-6} eV, and ionic relaxations were terminated when the residual forces between atoms reached less than 10^{-2} eV/Å. The plane-wave energy cutoff was set at 300 eV. One small change we made to the DFT settings compared to those of the original study is the use of the option `LASPH = .TRUE.` It signals to include non-spherical contributions from the gradient of the density inside the PAW spheres, since it is recommended by the VASP manual in case of van-der-Waals functionals.

The use of VASP entails that periodic boundary conditions (PBCs) apply in all our simulations. The real physical system that the simulation setup aims to model is, however, not fully periodic. PBCs can be physically motivated only for the graphene and substrate, along the two lateral directions a and b. They are unphysical for the AFM tip, and for the vertical direction c in general. To avoid spurious interactions introduced by the PBCs, parts that should not interact must be decoupled. This is achieved by choosing the lateral dimensions of the supercell sufficiently large, and by the inclusion of an empty volume, or 'vacuum gap', above the tip. The use of only a single point for sampling the third k-space direction, as mentioned earlier in

---

[2] Actually, in the case of iridium: the nearest-neighbor distance

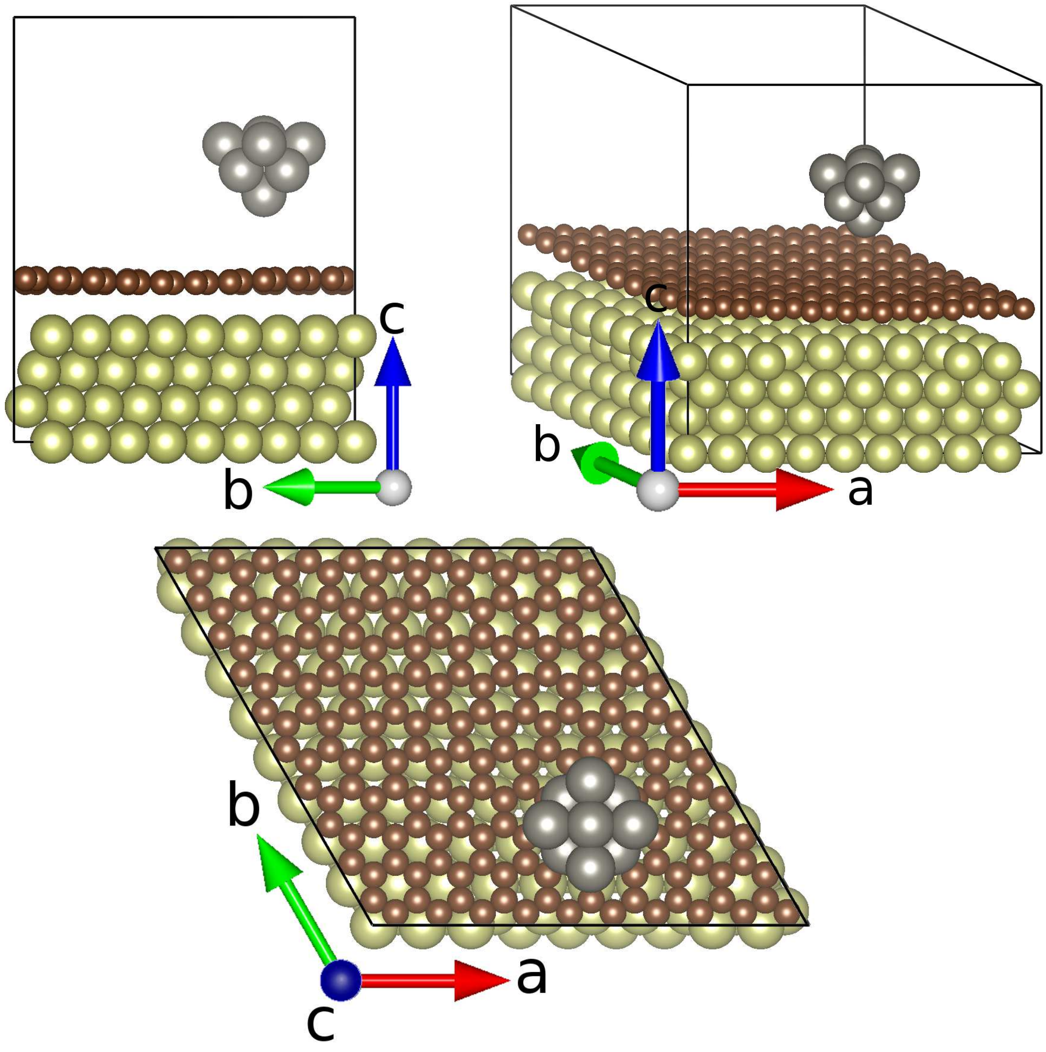

Fig. 3.1: Simulation cell viewed from different directions. Tungsten atoms are in gray, carbon in brown, iridium in yellow.

this section, can also be reasoned by the lack of true physical periodicity along the c direction.

Another consideration related to the PBCs is to make sure that the moiré formed by the graphene on iridium is not overly distorted as a result of enforcing a lateral periodicity of incorrect length. Experimentally, it has been found [68, 69] that the distance $l_{\text{moiré}}$ between two maxima of the moiré pattern (calculated from $1/l_{\text{moiré}} = 1/l_{\text{Gr}} - 1/a_{\text{Ir}}$) is about 9.3 times the iridium nearest-neighbor distance and about 10.3 times the repeat length l_{Gr} of the corrugated structure formed by the adsorbed graphene. The real moiré structure is therefore well represented by the supercell used, with its 9×9 iridium and 10×10 carbon structure, so this is not a concern.

Aside from VASP which provided the main simulation capability, we also used a number of other tools for various tasks. The VESTA program [70] was used for visualization of configurations. The python module *ase* (Atomic Simulation Environment) [71] was used for setting up configurations, and for post-processing and analysis. For performing 1D linear and non-linear fits, the python modules *scikit-learn* [72] and *lmfit* [73] were used. Tools used in the calculation of contact areas will be discussed at a later point in this chapter (Sec. 3.3).

3.2 Relaxations and separation control

We simulate the approach of the AFM tip at zero temperature, in a quasi-static fashion. This means that we are placing the tip at a number of different vertical positions, and for each of these positions the system is relaxed into its lowest-energy atomic configuration. This procedure requires that the positions of a subset of all atoms be held fixed during each relaxation, as there would be no way of controlling tip-sample separation if all atoms were allowed to move. The atoms kept fixed are the same for each tip position: they are those of the topmost tip layer and those of all four iridium substrate layers. The configuration of these fixed atoms is unchanged for all tip positions (save for global vertical translation of the tip, obviously). All remaining atoms (lower five tip atoms, whole graphene layer) are allowed to relax. This idealized description of the AFM tip's approach notably does not include effects of a compliant cantilever.

Note that in the case of the iridium substrate, more atoms are in fact held fixed than necessary for separation control alone. For that, the bottommost layer would be sufficient. Holding *all* substrate atoms in place is instead an approximation made for reasons of computational cost, since, unsurprisingly, relaxations involving fewer degrees of freedom proceed faster and converge more reliably. It is motivated by the fact that the graphene is only weakly bound to the substrate, with a binding energy of around 80 meV per carbon atom [59]. Relaxations of the substrate during tip movement are therefore not expected to have much of an impact on the graphene layer and, consequently, are neglected entirely.

On a technical level, the ionic relaxations were performed using the RMM-DIIS [74] and conjugate gradient [75] algorithms (options `IBRION = 1` and `IBRION = 2` in VASP, respectively). RMM-DIIS was mostly used for configurations presumed already close to the minimum, while for configurations presumed far away from the minimum the conjugate gradient algorithm was used for the first part of the relaxation, before finalizing it with RMM-DIIS.

Following Ref. [33], we adopt a scheme in which each tip position is characterized in terms of its so-called *static* and *relaxed* distance, denoted d_s and d_r, and both measured between the tip apex atom and the carbon atom directly underneath. The static distance, conceptually, is the distance that would be observed if there was no interaction between the tip and the graphene/substrate. For practical purposes, it is the distance measured in configurations that we create by relaxing both the tip and the graphene/substrate independently from one another (with the same atoms kept fixed as usual), as isolated subsystems, and then putting these subsystems together at some separation. The relaxed distance, on the other hand, is measured in the configuration obtained by relaxing the combined system. Thus, d_r represents the real approach between tip and graphene, but cannot be directly controlled in our method, whereas the value of d_s is less physically relevant but is what can actually be controlled when setting up the simulations. The relation between d_r and d_s gives some insight into the interaction regime that a given tip position falls into (see Fig. 3.2). At distances larger than the interaction range, $d_r = d_s$. Attractive interaction causes $d_r < d_s$, repulsive interaction leads to $d_r > d_s$.

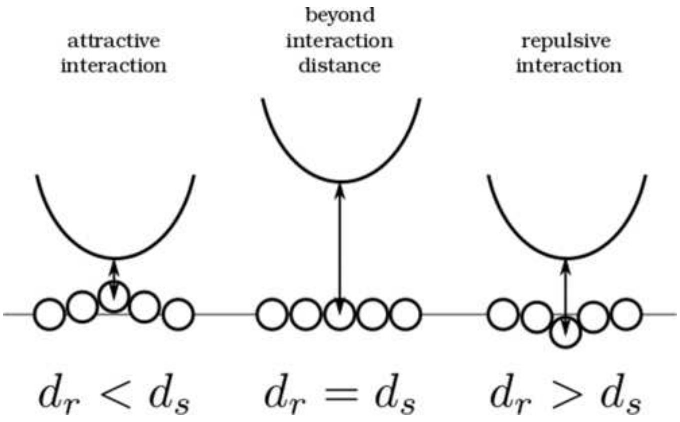

Fig. 3.2: Schematic relation between relaxed and static distance in different interaction regimes. Taken from Wolloch *et al.* [33].

The static distance d_s by construction never has a lateral component, because we place the tip with its apex atom exactly above the carbon atom below. By contrast, d_r can acquire a small lateral component because of displacements occurring during relaxation. However, these lateral components are negligibly small (see Appendix A) and, unless stated otherwise, values for d_r reported in this thesis are to be understood as the vertical component of d_r only. The lateral positions of the fixed tip atoms (tip base) never change throughout all tip positions.

Finally note that we are using d_s mostly just as a label of configurations. Its use does not imply that, for all tip positions, the relaxation was actually started in the initial configuration described above that defines d_s. For some tip positions, mostly ones far from the sample, this was indeed the procedure we used. But most relaxations were instead started from an initial configuration created by reusing the final relaxed configuration from another tip position relaxed earlier, and translating the tip up or down by a small increment (leaving its internal configuration and the configuration of the graphene unchanged). This was intended to reduce computation time taken by the relaxations as one starts out in a configuration presumably already closer to the relaxed one. In such an initial configuration, d_s obviously cannot be measured. What is ultimately relevant for controlling and setting the separation, however, is not d_s but the vertical position of the atoms that are held fixed during relaxation. Since d_s is uniquely related to the vertical position of the fixed tip atoms by a simple constant offset, we can still label each tip position with an equivalent value of d_s, and choose to do so because it has a certain intuitive quality.

3.3 Definition and calculation of contact area

The model of Ref. [33] for defining and calculating contact areas on the atomic scale is at the heart of this thesis too. It works as follows: The contact area between tip and sample, which is, *a priori*, not as well-defined on the atomic level as in a continuum theory, is defined in terms of the contact area between the constituting atoms, the building blocks of the two bodies. The problem is thus shifted to assigning a shape and spatial extent to the individual atoms, and defining the interfaces between them. For this, Bader's QTAIM (see Sec. 2.3) is used which assigns a region of space to each atom in the system based on properties of the electron density. The contact area between tip and sample is then naturally identified as the combined area of all interfaces shared by Bader atoms belonging to the tip and to the sample.

Having accepted this definition of the contact area, its identification and calculation is straightforward, in principle. But a challenge remains: the Bader atoms extend outward from the nuclei until they either meet another Bader volume or otherwise to infinity, owing to the fact that the electron density formally does not exactly fall to zero even at large distances from the nuclei. As a result, the Bader atoms of the tip and the surface are in contact with each other at any arbitrarily large separation, i.e., have a nonzero contact area at any separation. This is problematic since any sensible notion of contact demands that contact is only established for sufficiently close approach, not at all distances.

The issue is resolved by classifying regions of space with low electron densities n as vacuum. To that end, an electron density cut-off n_{cut} is defined and only points in space $\mathbf{r}$ where $n(\mathbf{r}) > n_{\text{cut}}$ are considered as belonging to a Bader atom, while all others are treated as vacuum. Doing so effectively truncates the Bader atoms at some distance from the nucleus, with larger values of n_{cut} resulting in smaller Bader atoms and vice versa. The exact value of n_{cut} is still left open to choice at this point. Since the resulting atomic shapes and calculated contact areas directly depend on it, it has to be be chosen based on some meaningful and unambiguous criterion. The choice of n_{cut} also determines at which separation the two bodies start being in contact. It is therefore inextricably linked to the fundamental question of what constitutes the onset of contact between two bodies.

In this context, a key idea of Wolloch *et al.* was to define the onset of contact in an unambiguous way by equating it with the so-called 'jump-to-contact'. The jump-to-contact, a phenomenon often seen in AFM experiments, marks the point during approach where strong interactions between tip and sample set in and significant relaxations first occur. It is detected in the simulation results by analyzing the two sets of distances d_r and d_s introduced in Sec. 3.2. When viewing d_r as a function of d_s, the jump-to-contact will be visible as a discontinuity in that curve. Based on this, n_{cut} is then tuned. On the one hand, it must be large enough that contact areas start being different from zero only after the jump-to-contact has occurred. On the other hand, it is chosen as low as possible while satisfying the former requirement, so as not to 'lose' any more electrons to the vacuum region than necessary.

Note that, importantly, this method for determining the onset of contact does not rely on external parameters. It works based on intrinsic properties extracted from the system itself, in the form of the relaxation behavior displayed by the system.

On the technical side of things, Bader's QTAIM has the desirable property that it interoperates easily with DFT, as the electron density is the central quantity in both formalisms. To perform the Bader partitioning we used a code from the University of Texas at Austin by Henkelman and co-workers [76–79]. Conveniently, this program can even operate directly on VASP charge density output files. We used it with the `neargrid` method, which is the default option. The Bader partitioning was run on the charge densities returned from VASP for the final relaxed configurations as follows. The charge densities in these final relaxed configurations were first recomputed on a fine grid of $432 \times 432 \times 448$ points to obtain good accuracy of the Bader partitioning and, by extension, of the contact areas. This constitutes a doubling of the number of points in each direction, compared to the default values that were used during the relaxation runs. The partitioning code only outputs the Bader volumes associated with each atom in the form of point clouds, but does not directly provide the surfaces bounding them. Therefore, to extract the contacting surfaces, those points are identified at which the two point clouds representing the combined Bader atoms of the tip and of the graphene/substrate are directly adjacent to one another. The value of the contact area is then found by first triangulating this set of points representing the interface, followed by calculating the area of the resulting surface. In carrying out these tasks of extracting and calculating the contact areas from the Bader partitioning output, we benefited from FORTRAN and MATLAB code provided by M. Wolloch.

3.4 Calculation of the load

Following the original approach of Ref. [33], we define the normal load as

$$L := -\frac{\partial E}{\partial d_r}, \tag{3.1}$$

where E is the total energy of the system and d_r is the relaxed distance introduced in Sec. 3.2. From our DFT simulations, we have $E(d_r)$ available at a set of discrete distances d_r. The simplest way to calculate the 1$^{\text{st}}$ derivative $E'(d_r)$ of the energy from this would be by a finite-differences scheme. Instead, our approach is to first fit some closed-form model function to the data points $E(d_r)$, and then to take its derivative analytically. This is likely more accurate than a finite-differences derivative because it is not as sensitive to data noise. Additionally, some physical insight might be gained from the values obtained for the model function's fit parameters.

4 Overview of the previous result

As mentioned in Chap. 1, a power-law behavior with an exponent of approximately 1/2 was found for the dependence of the real contact area on load in Ref. [33]. In this chapter, we briefly show how this was obtained for readers unfamiliar with the previous work, and also to better be able to later contrast our re-analysis with the original approach and findings.

The first step was to find an analytic expression for the dependence of A on d_r. It was proposed that $A(d_r)$ can be described by an exponential function

$$A(d_r) = A_\Delta \, \mathrm{e}^{-\lambda_r (d_r - \Delta_r)} \,, \tag{4.1}$$

where the parameters λ_r and Δ_r were determined from a fit to the seven data points with a nonzero value of A, i.e., below the 'jump-to-contact', that were available at the time. The constant $A_\Delta = 1\,\text{Å}^2$ is not a fit parameter, it serves only to ensure dimensional consistency.

The second step is the computation of the load, defined via the negative derivative of the energy-distance, recall Eq. 3.1. To compute the requisite derivative, a Morse potential [80]

$$E_M(d_r) = E_0 \left(\left[1 - \mathrm{e}^{-\gamma(d_r - d_0)}\right]^2 - 1 \right) \tag{4.2}$$

was first fit to the energy-distance curve. Only a few data points in a vicinity of the equilibrium distance were used in this fit. The only fit parameter is γ, while the depth E_0 of the potential and the equilibrium distance d_0 were fixed as the energy and the distance of the data point with the lowest energy. The load can be then computed by means of the differentiation of this fit function,

$$L(d_r) = -\frac{\partial E_M(d_r)}{\partial d_r} = -2\gamma E_0 \left[1 - \mathrm{e}^{-\gamma(d_r - d_0)}\right] \mathrm{e}^{-\gamma(d_r - d_0)} \,. \tag{4.3}$$

Solving Eq. 4.3 for d_r leads to

$$d_r(L) = d_0 - \frac{1}{\gamma} \ln \xi_\pm(L) \,, \tag{4.4}$$

with $\xi_\pm(L)$ a shorthand for[3]

$$\xi_\pm(L) = \frac{1 \pm \sqrt{1 + (2L)/(\gamma E_0)}}{2} \,. \tag{4.5}$$

Having now expressions for $A(d_r)$ in Eq. 4.1 as well as for $d_r(L)$ in Eq. 4.4, it is simply a matter of inserting the latter into the former to get an expression for $A(L)$,

$$\begin{aligned} A(d_r(L)) \equiv A(L) &= A_\Delta \,\mathrm{e}^{-\lambda_r(d_r(L)-\Delta_r)} \\ &= A_\Delta \,\mathrm{e}^{-\lambda_r(d_0-\frac{1}{\gamma}\ln\xi_\pm(L)-\Delta_r)} \\ &= \underbrace{A_\Delta \,\mathrm{e}^{-\lambda_r(d_0-\Delta_r)}}_{:=C,\ \text{indep. of L}} \underbrace{\mathrm{e}^{(\lambda_r/\gamma)\ln\xi_\pm(L)}}_{=[\xi_\pm(L)]^{\lambda_r/\gamma}} \,. \end{aligned} \tag{4.6}$$

With the values $\gamma = 4.11\,\text{Å}^{-1}$ and $\lambda_r = 4.19\,\text{Å}^{-1}$ obtained from the fits, the ratio λ_r/γ is close to 1 and therefore A is approximately proportional to ξ,

$$A(L) = C[\xi_\pm(L)]^{\lambda_r/\gamma} \simeq C\xi_\pm(L) = \frac{C}{2}\left[1 \pm \sqrt{1 + (2L)/(\gamma E_0)}\right] \,, \tag{4.7}$$

with $C = 24.15\,\text{Å}^2$. This corresponds to a power-law dependence of A on L with an exponent of $\simeq 1/2$, which is inferred by simply reading it from the expression.

Note that this result for $A(L)$ has been derived for distances close to the equilibrium distance, so may be assumed valid only for values of L close to zero.

---

[3] In Ref. [33], there is a typo, namely a minus instead of a plus sign is in front of the second term under the square root. However, this typo does not affect the fundamental finding of a 1/2-power dependence for the contact area.

5 Results and discussion

5.1 Ionic relaxations

Before discussing the contact area and its load dependence, we first give a brief overview of the behavior seen during the ionic relaxations, and of the resulting optimized configurations, at the different separations. While there is nothing fundamentally new about this compared to the original study in Ref. [33], we can give a fuller picture since we ran calculations at a more finely-spaced set of distances. Knowledge of the results from ionic relaxation will also be useful when later discussing the load-dependent contact areas, which is another reason to include it at this point.

At large separations, d_s and d_r are essentially equal since there are not yet any significant interactions between tip and graphene/substrate that would cause relaxations. Below around $d_s = 4\,\text{Å}$ there start to be some slight deviations from this linearity, with d_r going below d_s. A large and sudden decrease in d_r by about $0.7\,\text{Å}$ then occurs between $d_s = 3.63\,\text{Å}$ and $d_s = 3.59\,\text{Å}$ (see Fig. 5.1a), which we identify as the jump-to-contact as laid out in Sec. 3.3. At distances below the jump-to-contact, the dependence of d_r on d_s is again approximately linear, save for some nonlinearity in the vicinity of the jump-to-contact. However, d_r no longer decreases at the same rate as d_s, with d_r now varying more slowly. Consequently, there is a point where d_r, which after the jump-to-contact was initially smaller than d_s, becomes larger than d_s. Around this point, located at $d_s \approx d_r \approx 2.3\,\text{Å}$, the graphene transitions from bulging up toward the tip to being depressed down toward the substrate (see Fig. 5.3).

Analyzing separately the displacements of the tip apex and carbon atom below during relaxation (see Fig. 5.1b), it is seen that the carbon is responsible for most of the change in distance when passing from d_s to d_r. This is not surprising given that the graphene is only weakly bound to the substrate.

The equilibrium position of the tip over the sample, identified by the minimum of the relaxed configurations' energy as a function of distance (see Fig. 5.2), is found at $d_r \approx 2.25\,\text{Å}$, corresponding to $d_s \approx 1.85\,\text{Å}$. Note that this is not exactly the

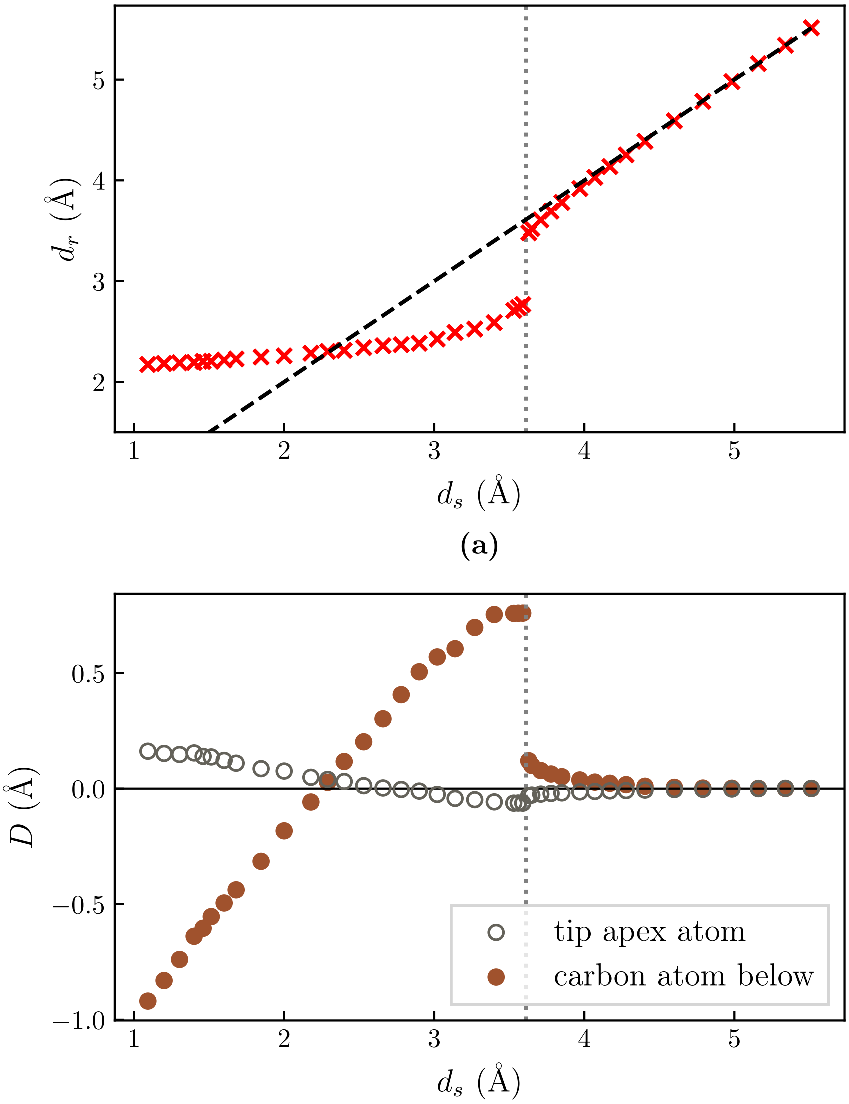

(a)

(b)

Fig. 5.1: Distances in the relaxed system as a function of static distance d_s. The approximate location of the jump-to-contact is indicated in both images by the vertical gray dotted line. **(a)** Relaxed distances d_r between the tip apex and the carbon atom situated directly beneath. The black dashed line visualizes the relation $d_r = d_s$ which describes the behavior at large separations. **(b)** Vertical displacements D of the tip apex atom and the carbon atom situated directly beneath, respectively, relative to their positions in the static configuration.

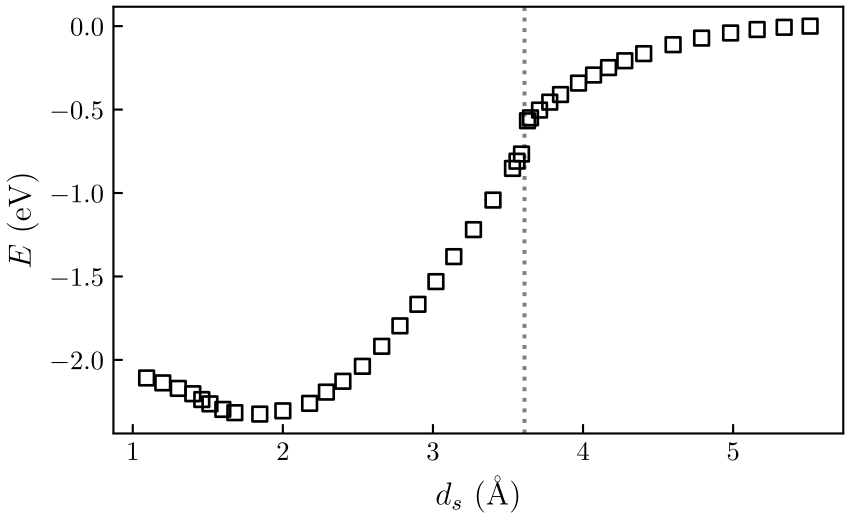

Fig. 5.2: Energy of the system in relaxed configurations, but shown as a function of static distance to be comparable with Fig. 5.1. The approximate location of the jump-to-contact is indicated by the vertical gray dotted line. Note that the energy is zero at the largest distance.

same position as where the graphene layer changes from arching up toward the tip to being indented by it, at $d_s \approx d_r \approx 2.3\,\text{Å}$, but very slightly below it.

When reducing d_s by only 0.02 Å, from $d_s = 3.63\,\text{Å}$ (our smallest successfully relaxed distance that is still above the jump-to-contact) to $d_s = 3.61\,\text{Å}$, we apparently entered a highly unstable region where we failed to obtain a relaxed configuration, i.e., fulfill the convergence criterion applied throughout that forces on all atoms are $< 10^{-2}\,\text{eV/Å}$ within a reasonable amount of time. At the point when we decided to abandon the relaxation attempt for this distance, the tip-carbon distance was at 2.82 Å and still continuing to fall. The distance $d_s = 3.61\,\text{Å}$ is thus not included in any of the results shown. We had initially believed that by reusing relaxed configurations as initial configurations for relaxing the next smaller distance, as described in Sec. 3.2, and by proceeding in small increments of d_s, we would be able to resolve in more detail the relaxation happening at the jump-to-contact. Instead, what we conclude is that the jump-to-contact is very sudden and indeed deserving of its name, and that there is a range of relaxed distance values that is not feasible to access, in terms of computation time and required smallness of d_s increments.

Within our calculations, there were a few distances which displayed the behavior that when going from one static distance value d_s to the next smaller one, the relaxed distance d_r actually *increased* compared to the previous one, even if just by a few hundredths of an Ångström. Since this is highly counterintuitive, we suspected it might be a sign of an imperfect relaxation that got stuck in a metastable mini-

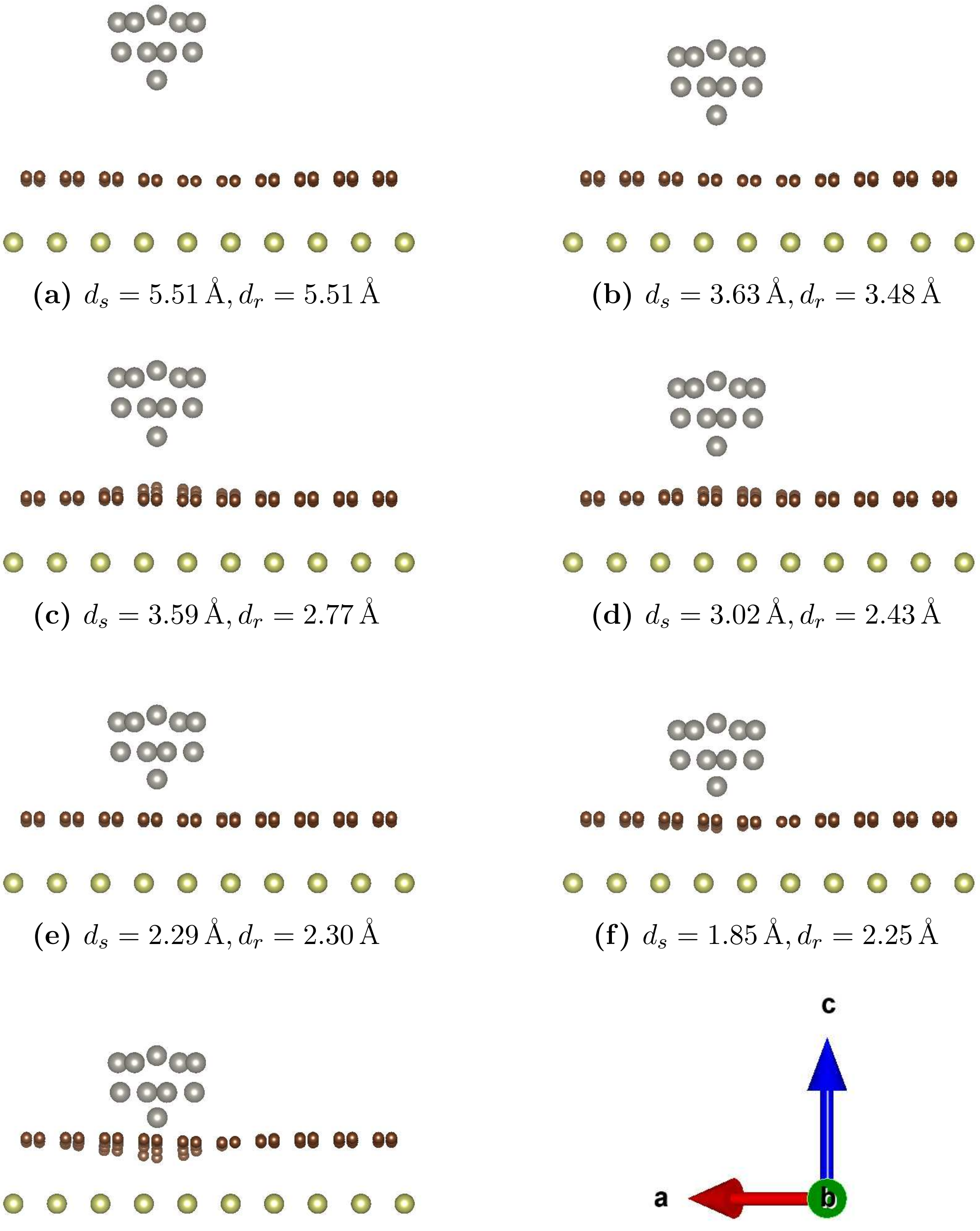

(a) $d_s = 5.51\,\text{Å}, d_r = 5.51\,\text{Å}$

(b) $d_s = 3.63\,\text{Å}, d_r = 3.48\,\text{Å}$

(c) $d_s = 3.59\,\text{Å}, d_r = 2.77\,\text{Å}$

(d) $d_s = 3.02\,\text{Å}, d_r = 2.43\,\text{Å}$

(e) $d_s = 2.29\,\text{Å}, d_r = 2.30\,\text{Å}$

(f) $d_s = 1.85\,\text{Å}, d_r = 2.25\,\text{Å}$

(g) $d_s = 1.20\,\text{Å}, d_r = 2.18\,\text{Å}$

Fig. 5.3: Side view at selected stages of approach. The axes apply to all plots. The depicted configurations are relaxed but labeled with both static and relaxed distance. **(a)** Large distance where essentially no interaction occurs. **(b)** Smallest distance at which still no jump-to-contact occurred. **(c)** Directly after jump-to-contact. **(d)-(g)** Upon further approach the bulging upward of the graphene reduces until it starts being depressed toward the substrate. The configuration in **(f)** is close to the equilibrium, whereas that in **(g)** is compressed beyond it.
This figure was created using VESTA [70].

mum. To investigate and alleviate this, for a few distances we reran the relaxations starting from a different initial configuration than during the first attempt. Indeed, more sensible results and lower energies were obtained. Due to time constraints, we performed this kind of sanity check only for a few distances. However, in light of this observation we must certainly keep in mind the possibility that some results may be affected by imperfect relaxations. Candidates where we suspect this may be the case are the two sets of three distances each, directly below the jump-to-contact, which seem to behave in a 'stepwise' manner (see Fig. 5.1a).

Precise values for static and relaxed distances at all tip positions can be found in Appendix A.

5.2 Contact areas

Having done calculations at a larger number of distances than in the original study means we also narrowed down the location of the jump-to-contact a bit more. Since the cutoff electron density in the Bader partitioning is chosen based on the requirement that contact areas be nonzero only below the jump-to-contact (see Sec. 3.3), we found we had to slightly adapt its value to still be consistent with our additional data. The old value of $n_{\mathrm{cut}} = 5.0 \times 10^{-2}\,\mathrm{electrons/\mathring{A}^3}$ from Ref. [33] led to a finite contact area even at our smallest distance above the jump-to-contact (at $d_s = 3.59\,\mathring{\mathrm{A}}$). We settled for a minimally larger cutoff at $n_{\mathrm{cut}} = 5.25 \times 10^{-2}\,\mathrm{electrons/\mathring{A}^3}$ to ensure that contact areas are nonzero only below the jump-to-contact. This is the value that will be used throughout the remainder of this thesis. Raising the cut-off of course slightly enlarges the vacuum region and therefore increases the number of electrons assigned to it. However, the change is small and across all distances studied, the largest number of electrons assigned to the vacuum region was 33.7 out of a total of 3776 electrons, which we deem still very acceptable. Contact areas also become slightly smaller as a result. Precise values for both cutoff densities can be found in Appendix A.

Otherwise our computation of the contact areas follows that in the original study, and we have nothing new to report about it. The contact areas are displayed as a function of distance in Fig. 5.4, and their surface profiles at selected distances are depicted in Fig. 5.5.

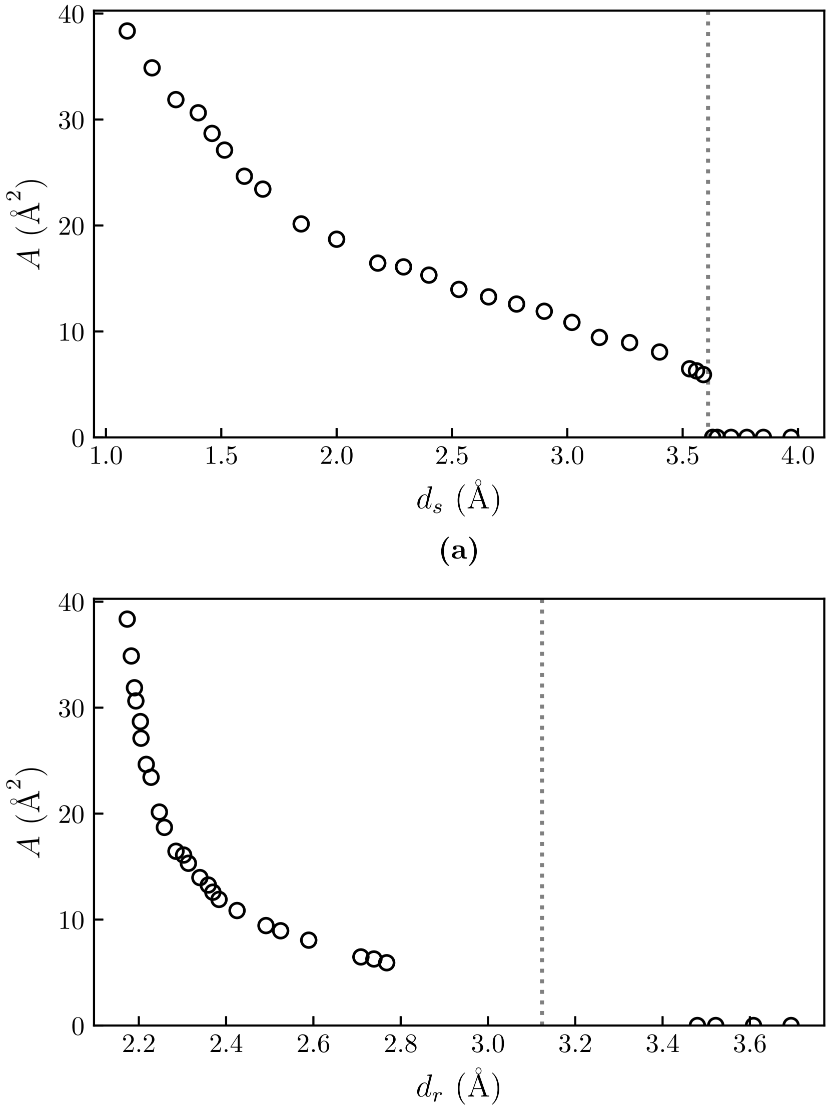

(a)

(b)

Fig. 5.4: Contact area as a function of **(a)** static and **(b)** relaxed distance. The vertical gray dotted line indicates the approximate location of the jump-to-contact.

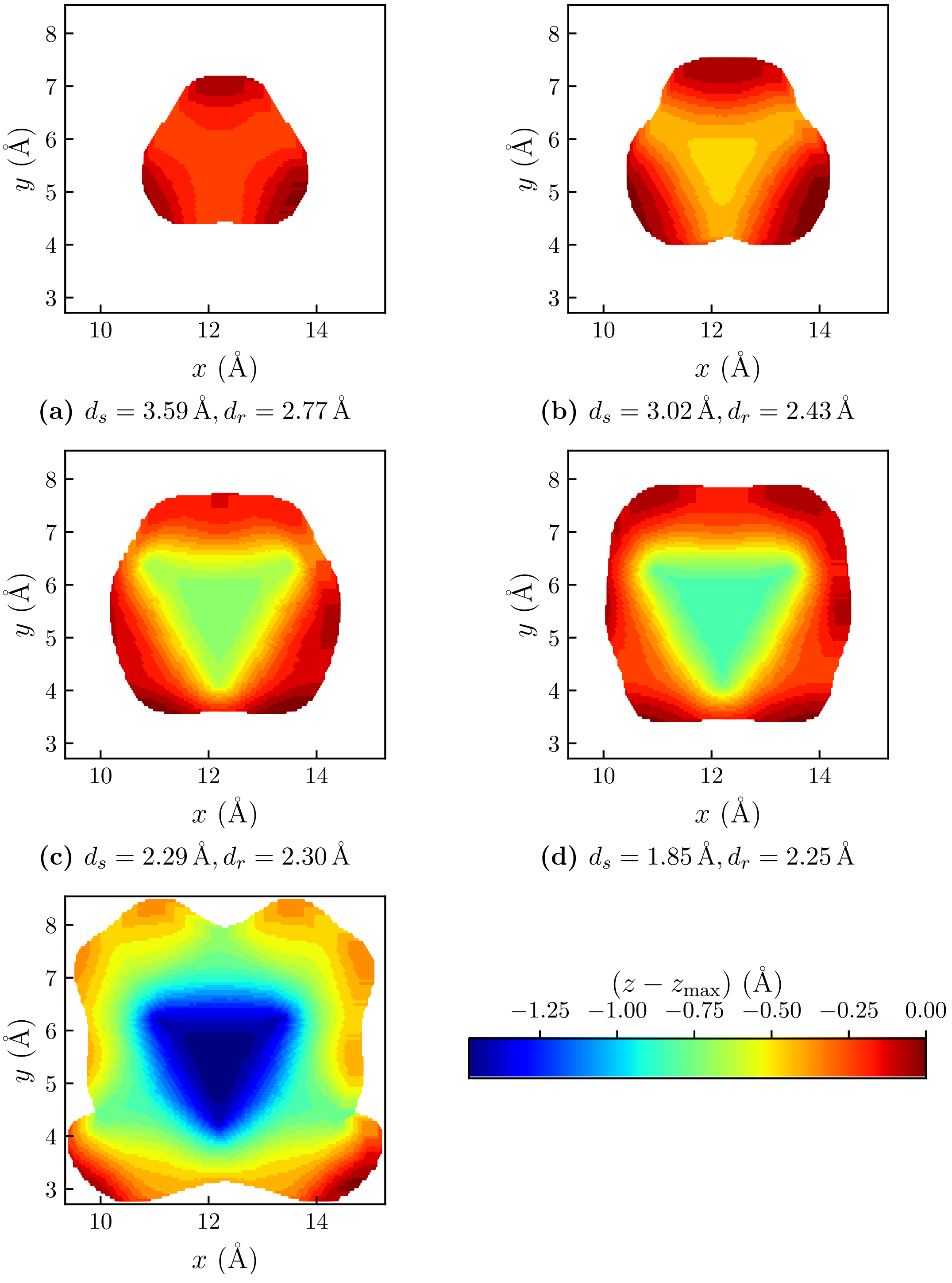

(a) $d_s = 3.59\,\text{Å}, d_r = 2.77\,\text{Å}$

(b) $d_s = 3.02\,\text{Å}, d_r = 2.43\,\text{Å}$

(c) $d_s = 2.29\,\text{Å}, d_r = 2.30\,\text{Å}$

(d) $d_s = 1.85\,\text{Å}, d_r = 2.25\,\text{Å}$

(e) $d_s = 1.20\,\text{Å}, d_r = 2.18\,\text{Å}$

Fig. 5.5: Surface profiles $z(x, y)$ of the contact areas, shown relative to the highest point z_{max} of each surface. The distances included are all those from Fig. 5.3 with a nonzero contact area. The cartesian coordinate x corresponds to direction a from Fig. 3.1, the z coordinate to direction c. The color scale included at the bottom right applies to all plots.

5.3 Load calculations

As laid out previously in Sec. 3.4, we calculate the load as the negative 1st derivative of E w.r.t. d_r, and to evaluate the derivative we first fit a model function to the discrete data points $E(d_r)$. So, the problem of calculating the load is essentially that of choosing a suitable fit function and obtaining a good fit to the data. Naturally, to decide what fit function(s) might be appropriate, we first took a look at the shape of E as a function of d_r. This curve is shown in Fig. 5.6.

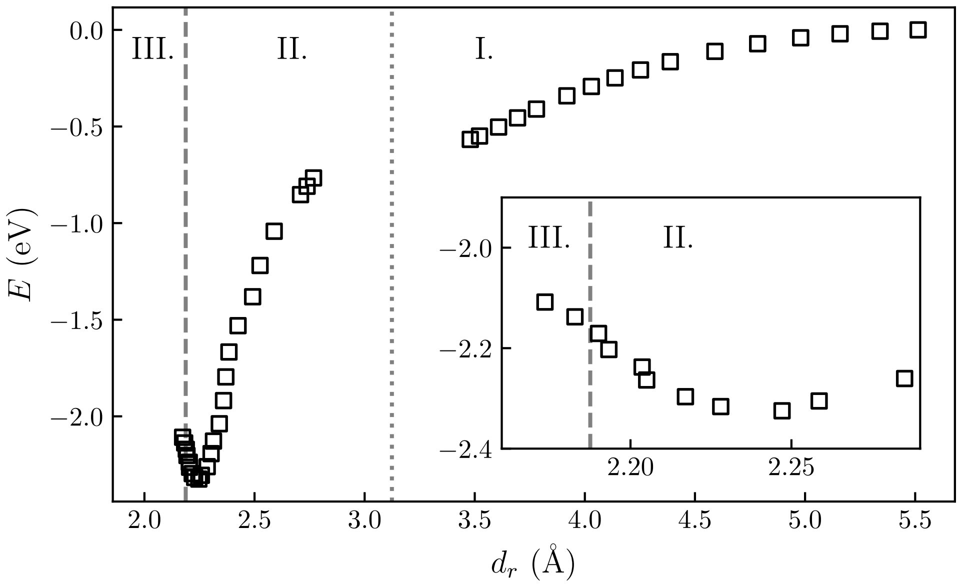

Fig. 5.6: Different regimes identifiable in the relation between energy and relaxed distance. The inset shows the region of transition between II. and III.

Broadly, we identify three regimes in the $E(d_r)$ curve:

In the distance range above the jump-to-contact (labeled I. in Fig. 5.6), there is a region of attractive interaction that we attribute mainly to long-range van-der-Waals interactions. Below the jump-to-contact, there is a region (labeled II. in Fig. 5.6) where the interaction could (qualitatively) be called 'Lennard-Jones-like', in the sense that it consists of an attractive and a repulsive section, with an equilibrium in between. At the transition between regions I. and II., a gap along the d_r axis can be seen in the data points. This is due to the sudden strong relaxations at the jump-to-contact, which make it hard to control d_r in this region: For tip positions slightly above the jump-to-contact, there is no strong relaxation yet, causing the data points to remain to the right of the transition region in Fig. 5.6. But for tip positions even just slightly below the jump-to-contact, strong relaxations occur and cause the corresponding data points to move far to the left of the transition region in Fig. 5.6, as the system seeks on its own to reduce the separation.

Lastly, there is a third region at smaller distances (labeled III. in Fig. 5.6), that we did not probe into very far. It is marked first by a slowdown of the increase of $E(d_r)$ with decreasing distance d_r (seen in our data in Fig. 5.6), before $E(d_r)$ then levels out and even starts to fall again with decreasing d_r (not seen in our data because we did not go to distances that small, but found in the past in Ref. [33]). This behavior has been attributed in Ref. [33] to the formation of chemical bonds between the tip and the iridium substrate. This is in contrast to a Lennard-Jones-like or similarly shaped interaction potential that would continue to increase more and more steeply as the distance is reduced below the equilibrium.

Knowing the values of L in region I. is not required for the analysis of the load-dependent contact area $A(L)$ since, by definition, the contact areas are identically zero above the jump-to-contact, anyway. So, strictly speaking, we do not need to calculate the derivative of $E(d_r)$ in this region, and therefore do not need to make a fit to the data. This is not to say the behavior of $E(d_r)$ in region I. is irrelevant to us, since insight about the physics of the system might still be gained from it.

As a fit function in region II. we intend to use a *generalized m-n Lennard-Jones* (LJ) potential[4]

$$U_{\mathrm{LJ}}^{m\text{-}n}(d_r) = -\frac{E_0}{m-n}\left[m\left(\frac{d_0}{d_r}\right)^n - n\left(\frac{d_0}{d_r}\right)^m\right], \tag{5.1}$$

where d_0 denotes the equilibrium distance and $E_0 > 0$ the depth. The generalized LJ potential has the exponents m and n as adjustable parameters. This distinguishes it from the more common 'standard' LJ potential, most often referring to the special case of Eq. 5.1 with (m, n) fixed to $(12, 6)$. It is our hope that this potential, having two shape-controlling parameters rather than only one, will allow us to capture the behavior of $E(d_r)$ a bit more fully than the Morse potential used in the past in Ref. [33].

Finally, the region III. will not be included in our analysis. There are multiple lines of reasoning behind this:

1. From a purely practical point of view, inclusion of region III. in our analysis would complicate the search for a suitable fit function for $E(d_r)$. For energy-distance curves qualitatively like that in region II., functional forms are well-established, e.g. Lennard-Jones-like potentials or the Morse potential used in the past in Ref. [33]. But the behavior seen in our system at small distances would require a different description, which we want to avoid for now.

---

[4] Sometimes also referred to as a *Mie* potential [81].

2. One of the main questions of this thesis is the comparison of $A(L)$, found with the *ab-initio* approach, with classical continuum models of contact mechanics widely used in the interpretation of atomic-scale FFM measurements. Now, it is already clear from the outset that the behavior of $A(L)$ in region III. does not fit common continuum models: An interaction potential $E(d_r)$ like that in region III. leads to a *third* branch of the $A(L)$ curve. This is illustrated schematically in Fig. 5.7. Common continuum model predictions for $A(L)$ lack this feature (cf. Fig. 2.2). For comparison with continumm models, we therefore restrict ourselves only to the region where the behavior of $A(L)$ may be expected in the first place to be (at least qualitatively) similar to these models. This means restriction to region II.
3. More fundamentally, we believe that there will be a point at small separations where it no longer makes sense to think of the tip and graphene/substrate as two distinct bodies. One may still use the Bader partitioning scheme to calculate contact areas between the individual involved atoms. But the notion of the tip and the graphene/substrate as conceptually separate bodies, and thus that of a contact area between them, probably stops being meaningful at some point. And while at this time we do not offer a definition of when this occurs, the onset of chemical bonding between the tip and the iridium, and the related behavior seen in $E(d_r)$ in region III., seem like a possibility.

For the transition between regions I. and II. there is an unambiguous criterion, namely the jump-to-contact (see Secs. 3.3 and 5.1). It is comparatively less clear where exactly the transition from region II. to III. should be located. For now, we choose the point where the slope of $E(d_r)$ starts to decrease when reducing d_r (i.e., the point of inflection, corresponding to point c in Fig. 5.7), and we identify this point only roughly by eye. This choice amounts to excluding the two lowest values of d_r in our data from the fits (see the inset of Fig. 5.6). However, we do not find this entirely satisfactory. For future studies, a more objective criterion would be desirable, based perhaps on an analysis of charge accumulation upon chemical bond formation between tip and substrate.

5.3.1 A first fitting attempt

In this section, we briefly report on an attempt to make fits to the energy-distance data, from a very early stage of our work. This is only to illustrate our thought process, as this early attempt was based on an initial belief about the shape of the $E(d_r)$ curve that turned out to be incorrect, and we ultimately did not pursue it.

Early on — when there were much fewer data points available than shown in the plots included in this thesis — it had looked to us as if there might be a second,

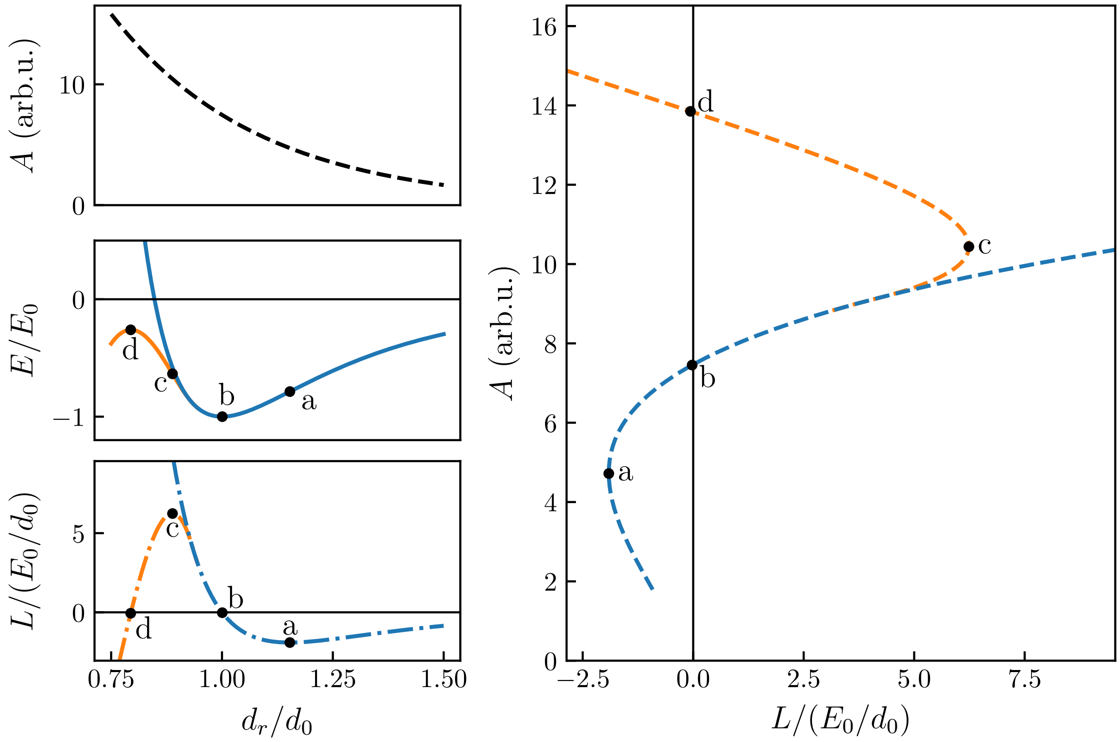

Fig. 5.7: Schematic correspondence between special points on the $E(d_r)$, $L(d_r)$ and $A(L)$ curves. Shown for an assumed exponential form of $A(d_r)$, and two different prototype interaction potentials $E(d_r)$, a LJ-like one with depth E_0 and equilibrium distance d_0 (blue), and one that deviates from the LJ-like form and turns attractive again at small distances (orange). a, b: Point of most negative load and equilibrium position in LJ-like potential. c: Point of most positive load for potential deviating from LJ-like form. d: Point where deviating potential becomes again attractive.

shallower, minimum in $E(d_r)$ somewhere around $d_r \approx 3\,\text{Å}$, in addition to the main minimum at $d_r \approx 2.25\,\text{Å}$. At the time we had also still intended to fit $E(d_r)$ both above and below the jump-to-contact with one single fit function. It was believed that the presence of such a second minimum, which is not present in common model potentials, like the m-n Lennard-Jones or Morse potential, would be the main challenge in describing $E(d_r)$ with a reasonably simple fit function. This led us to search for tip-surface interaction potentials with a second minimum perhaps already proposed in the literature.

Our brief search did not turn up any such potential that had been specifically proposed as a surface interaction potential. However, a class of potentials that can produce the desired shape, termed *Lennard-Jones-Gauss* (LJG) potentials, was found in the context of a different application. Potentials of this type were introduced in Refs. [82, 83] as model interparticle pair potentials for studying self-assembly and stability of crystalline and quasi-crystalline structures. In this original context, LJG potentials could be motivated as being an approximation to the first few oscillations of the characteristic oscillatory tails (Friedel oscillations [84]) seen in interatomic pair potentials in metals. For our needs we repurpose them as tip-surface interaction potentials.

In general, LJG potentials are obtained by combining a Lennard-Jones-type potential with one or several additional Gaussian terms. For our application we use a variation of LJG potential given by

$$U_{\mathrm{LJG}}^{m\text{-}n}(d_r) := U_{\mathrm{LJ}}^{m\text{-}n}(d_r) - E_G \exp\left(-\frac{(d_r - d_G)^2}{2\sigma_G^2}\right) . \tag{5.2}$$

It consists of the generalized m-n Lennard-Jones potential $U_{\mathrm{LJ}}^{m\text{-}n}(d_r)$, given by Eq. 5.1, and a Gaussian-well term with parameters E_G, d_G and σ_G. A fit of such a LJG potential to our data (including also all our more recent data) is shown in Fig. 5.8.

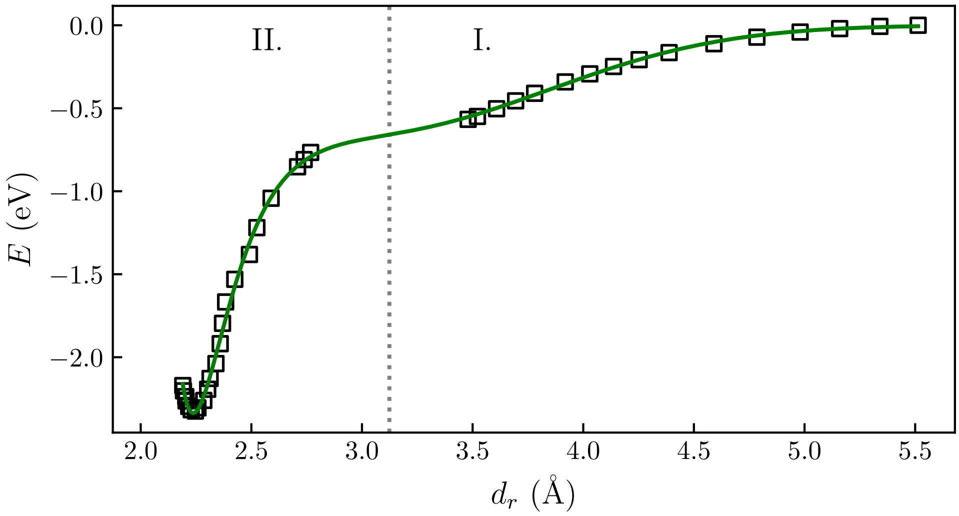

Fig. 5.8: Fit of a Lennard-Jones-Gauss potential Eq. 5.2 to the E-vs-d_r curve. Regions I. and II. from Fig. 5.6 were included in this fit. Vertical dotted line indicates approximate location of jump-to-contact.

But as said already at the beginning, we did not pursue the LJG route further. There are indeed several issues with it. With more data becoming available as our calculations progressed, we did not actually observe the initially expected second minimum. What we had interpreted as a hint at a second minimum is instead the discontinuity in the data around the jump-to-contact. There is therefore no real need for the LJG description in the first place. Moreover, the LJG fit suffers from a lack of interpretability, because of the large number of fit parameters and the lack (at least in the context where we apply it) of a theoretical justification for the Gaussian form. We are also more generally skeptical about using one single function for fitting across the jump-to-contact at all, given the observed abruptness of the jump-to-contact (see Sec. 5.1) and the fundamental change in interaction regime that this points to.

5.3.2 Van-der-Waals background

Given our belief that the jump-to-contact signals a profound shift in the tip-surface interaction regime, we do not expect that indiscriminately using a single fit function for $E(d_r)$ across the jump-to-contact, as in the early fitting attempt made in Sec. 5.3.1, will lead to a very good or physically interpretable parameterization of $E(d_r)$. Therefore, we hoped to refine the analysis by treating the region below the jump-to-contact separately, while still incorporating possibly relevant physical information from the region of large tip-sample separations, as outlined below.

Above the jump-to-contact, we assume that the interaction is dominated by long-range van-der-Waals interactions. Below the jump-to-contact, where tip and surface are in contact, we expect that additional short-range interactions are present, at least partly of chemical type. There is, however, no reason to believe that van-der-Waals interactions stop being relevant at small distances. So the total interaction potential $E(d_r)$ in this region will be due to a combination of both the still-present 'van-der-Waals background' $E_{\text{vdW-bg}}(d_r)$ and short-range interactions superimposed on top of it. We assume that an improved description and understanding of $E(d_r)$ at small distances may be obtained by subtracting the 'van-der-Waals background' from it so that the remaining short-range contributions to $E(d_r)$ can then be analyzed and interpreted on their own. Of course, this assumption of clear separability into long-range van-der-Waals and short-range contributions involves some degree of idealization. To decide whether the attraction below the jump-to-contact (with or without having subtracted some sort of background) is of van-der-Waals type, one can look at whether the attractive exponent obtained from fitting the m-n LJ potential Eq. 5.1 in this region is consistent with a van-der-Waals interaction.

In our attempt to extract and remove this 'van-der-Waals background', we intended to do the following: We first separately consider the region of large tip-sample separations d_r, where we expect van-der-Waals interactions to be dominant. To infer the functional form and magnitude of $E_{\text{vdW-bg}}(d_r)$, we then wanted to fit some theoretically known functional form of a van-der-Waals interaction energy to our data points in this distance region. The obtained van-der-Waals energy contribution

$E_{\text{vdW-bg}}(d_r)$ can then be extrapolated to small distances and subtracted from $E(d_r)$ in that region.

In practice, this approach requires making a choice for the van-der-Waals function used for fitting the data at large distances. Unfortunately, we realized that we are not entirely confident as to what is the most appropriate choice, and that there is some ambiguity involved. The following is a brief overview of some considerations.

The simplest theory for obtaining van-der-Waals interaction energies of extended bodies is that by Hamaker [85, 86], which is based on the assumption of pairwise additivity of the interatomic van-der-Waals pair potential $w(r) = -C/r^6$ for all atoms. For the interaction energy between two spheres with radii R_1 and R_2, at a separation d between their surfaces, this theory gives

$$\begin{aligned} E_{\text{vdW}}^{\text{sph-sph}}(d) = -\frac{H}{6}\Bigg\{ & \frac{2R_1R_2}{(2R_1+2R_2+d)d} + \frac{2R_1R_2}{(2R_1+d)(2R_2+d)} \\ & + \ln\left[\frac{(2R_1+2R_2+d)d}{(2R_1+d)(2R_2+d)}\right]\Bigg\}, \end{aligned} \tag{5.3}$$

with the Hamaker constant $H := \pi^2 C\rho_1\rho_2$, where ρ_1, ρ_2 are the numbers of atoms per unit volume within the two spheres. If one now considers a sphere of radius R and a flat surface (i.e., $R_1 \equiv R$ and $R_2 \to \infty$), as a model for the AFM tip and sample, Eq. 5.3 simplifies to

$$E_{\text{vdW}}^{\text{sph-surf}}(d) = -\frac{H}{6}\left\{\frac{R}{d} + \frac{R}{2R+d} + \ln\left[\frac{d}{2R+d}\right]\right\}, \tag{5.4}$$

with the limiting-case behavior $E(d) \propto -1/d^3$ for $d \gg R$ and $E(d) \propto -2/d$ for $d \ll R$. If we were to use Eq. 5.4 as the model function to fit to our data, we would set $d = d_r$, and the Hamaker constant H would naturally take the role of a fit parameter that characterizes the interaction. Now, one may say that the shape of the tip in the model system under study is not optimally described by a sphere at all. One alternative might be a conical tip, for which, too, expressions for the van-der-Waals interaction with flat surfaces have been derived [87]. But even so, accounting for the tip shape is not the only problem in choosing an appropriate fit function for extracting the van-der-Waals background. A perhaps greater issue is the layeredness of the sample. From this, additional complications arise regarding the choice of fit function, the interpretation of the resulting fitted van-der-Waals interaction energy, and how to correctly extrapolate the different layers' contributions to below the jump-to-contact.

While these may be solvable problems in principle, we deemed it probably not worth the effort. So, instead of explicitly extrapolating $E_{\text{vdW-bg}}(d_r)$ to below the jump-to-contact in the form of a d_r-dependent function, we went for a more pragmatic strategy, which will be the topic of the next section.

5.3.3 Approximate treatment of van-der-Waals background

In the previous section we have said that we are not sure about the correct functional form to use for extracting the van-der-Waals background from the long-range behavior of $E(d_r)$ and extending it to below the jump-to-contact. But we still believe that there is merit to using such a description for $E(d_r)$. We therefore took a more pragmatic approach for taking the influence of the van-der-Waals interactions below the jump-to-contact into account. It consists simply of complementing the m-n LJ potential Eq. 5.1 with a constant offset $E_{\text{vdW-bg}}$, to approximately account for any remaining influence of van-der-Waals interactions below the jump-to-contact, before we fit it to the data in region II. We fix the value of this offset to the energy of our last data point above the jump-to-contact, at $d_r = 3.48\,\text{Å}$. This gives $E_{\text{vdW-bg}} = -0.57\,\text{eV}$ (as always measured relative to the energy at our largest distance). For the nonlinear least-squares fits performed in this section, Python's *lmfit* module [73] was used. See Appendix C for more technical details on the fits.

At first, in order to keep down the number of fit parameters, we did a fit with only the exponents m and n as fit parameters, with the depth E_0 and equilibrium distance d_0 of the LJ potential fixed to the values taken directly from the lowest-energy data point. This fit led to the curious result of almost identical values for m and n, at $m \approx n \approx 18$ (see Tab. 5.1). Due to the unusualness of $m \approx n$ in a LJ-type potential, and since for m close to n the denominator in Eq. 5.1 becomes very small, which could create numerical issues, we initially suspected this to be an unphysical result caused by some problem with the nonlinear optimization routine. However, visually, the fit looked reasonable (see Fig. 5.10). So, as a plausibility check, we simply manually varied m and n in integer steps within some range and evaluated the deviation of the fit function from the data points for each parameter combination. Having only two adjustable parameters m and n, this is very doable. The result is shown in Fig. 5.9 and also points to $m \approx n$ and a value around 17 or 18. In light of this, we considered the possibility that the best description of our data in terms of an m-n LJ potential really is provided by $m = n$. Indeed, if we calculate the limit[5]

$$U^n_{\text{LJ-lim}}(d_r) := \lim_{m \to n} U^n_{\text{LJ-lim}}(d_r) = -E_0 \cdot \left[1 - n \ln\left(\frac{d_0}{d_r}\right)\right] \cdot \left(\frac{d_0}{d_r}\right)^n , \tag{5.5}$$

---

[5] The idea of $m = n$ in a LJ-like potential may seem bewildering at first. However, the key point is that Eq. 5.1 is formulated explicitly in terms of the depth E_0 and equilibrium distance d_0, which forces the prefactors to be not independent of m and n. A meaningful limit $m \to n$, while keeping E_0 and d_0 constant, can therefore be calculated.

and then do the same fit as before with this new function $U^{n}_{\text{LJ-lim}}$, we find the results from fitting the full $U^{m\text{-}n}_{\text{LJ}}$ reproduced (see Tab. 5.1). The calculation of the limit $U^{n}_{\text{LJ-lim}}$ is shown in detail in Appendix B.

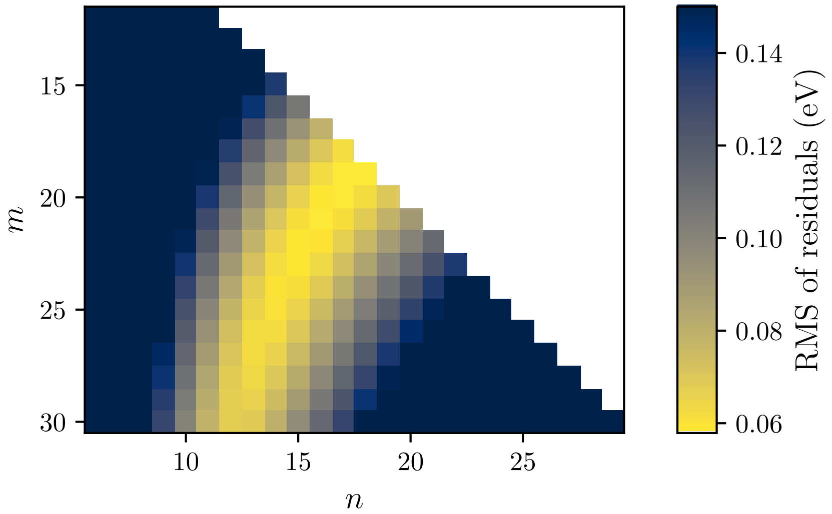

Fig. 5.9: Root mean square (RMS) of residuals between $U^{m\text{-}n}_{\text{LJ}}(d_r) + E_{\text{vdW-bg}}$ and the DFT data points $E(d_r)$ in region II. Exponents m, n varied, while E_0, d_0 fixed to values taken directly from the data. Includes only $n < m$. The case $n > m$ is equivalent due to symmetry of Eq. 5.1 under exchanging m and n, and $m = n$ would lead to division by zero in Eq. 5.1.
Note that the color representation goes into saturation for larger RMS values in order to make differences at small values more easily visible.

Tab. 5.1: Parameters from fits to $E(d_r)$ with Eqs. 5.1 and 5.5, for E_0 and d_0 fixed to their values taken directly from the data.

fit function	m	n	E_0 (eV)	d_0 (Å)
$U^{m\text{-}n}_{\text{LJ}}(d_r) + E_{\text{vdW-bg}}$	18.191	18.190	1.76 (fixed)	2.25 (fixed)
$U^{n}_{\text{LJ-lim}}(d_r) + E_{\text{vdW-bg}}$	n.a.	18.2	1.76 (fixed)	2.25 (fixed)

We also checked what happens when treating E_0 and d_0 as adjustable fit parameters as well, rather than fixing them beforehand to the values taken from the lowest-energy datapoint $E(d_r)$. We tried this for both fit functions $U^{m\text{-}n}_{\text{LJ}}(d_r)$ and $U^{n}_{\text{LJ-lim}}(d_r)$. It appears that letting E_0 and d_0 vary, too, leads to an improved description of the data in the repulsive region (below the minimum). Whereas the fits with fixed E_0 and d_0 predict systematically larger values than the data points in this region, this is not the case anymore when E_0 and d_0 are varied in addition to m and n (see Fig. 5.10) The differences may not be large in absolute terms, but will be amplified when taking the derivative of E w.r.t. d_r, which is what we are ultimately interested in. Since we see no downside to letting E_0 and d_0 vary as well, we will proceed this way.

When fitting $U_{\mathrm{LJ}}^{m\text{-}n}(d_r)$ to the data while letting E_0 and d_0 vary we no longer find that the fit results in $m \approx n$ (see Tab. 5.2). But the curves resulting from $U_{\mathrm{LJ}}^{m\text{-}n}(d_r)$ and $U_{\mathrm{LJ\text{-}lim}}^{n}(d_r)$ continue to be quite similar (see Fig. 5.10). An appealing feature of the limit version $U_{\mathrm{LJ\text{-}lim}}^{n}(d_r)$ is that its shape-controlling parameter n appears to be much less sensitive to the fixing of E_0 and d_0 than the two parameters m and n of $U_{\mathrm{LJ}}^{m\text{-}n}(d_r)$ (compare Tab. 5.1 with Tab. 5.2).

Tab. 5.2: Parameters from fits to $E(d_r)$ with Eqs. 5.1 and 5.5, for E_0 and d_0 allowed to vary in addition to m and n.

fit function	m	n	E_0 (eV)	d_0 (Å)
$U_{\mathrm{LJ}}^{m\text{-}n}(d_r) + E_{\mathrm{vdW\text{-}bg}}$	27.1	13.0	1.77	2.24
$U_{\mathrm{LJ\text{-}lim}}^{n}(d_r) + E_{\mathrm{vdW\text{-}bg}}$	n.a.	17.8	1.76	2.24

Unfortunately, we do not have much to offer in the way of interpretation of the Lennard-Jones exponents obtained from the fits. The fact that the attractive exponent n obtained after subtracting $E_{\mathrm{vdW\text{-}bg}}$ is not somewhere in the range ≤ 6 might be interpreted as a hint that the interaction below the jump-to-contact is not, or at least not dominantly, of van-der-Waals type. The obtained repulsive exponents m are considerably greater than the value 12 in the standard 12-6 LJ potential, commonly associated with Pauli repulsion in interatomic interactions[6]. What needs to be said about this is firstly that the repulsive region within our data spans only a fairly small range of d_r values, so the estimates for the repulsive exponent might not actually be too reliable. Secondly, it might not even make sense to apply such an interpretation to the exponent values at all, since in our case we use the LJ potential not to describe interatomic interactions but a tip-surface interaction involving many atoms, which likely poses additional complications. Concerning the m-n LJ potential with $m = n$ that we found when keeping E_0 and d_0 fixed, we are unaware of any mention of such a potential in the literature (which is most likely just a failure on our part to search in the right places), and are unsure about any physical interpretation of it. So, ultimately, the fits must be seen as just a mostly heuristic representation of $E(d_r)$ to help with the load calculations.

---

[6] Note, however, that there is no theoretical basis for the description of the repulsive part with such an inverse-12th-power expression [88, 89]. It is used solely for ease and speed of computation since it can be calculated by squaring the attractive 6th-power term.

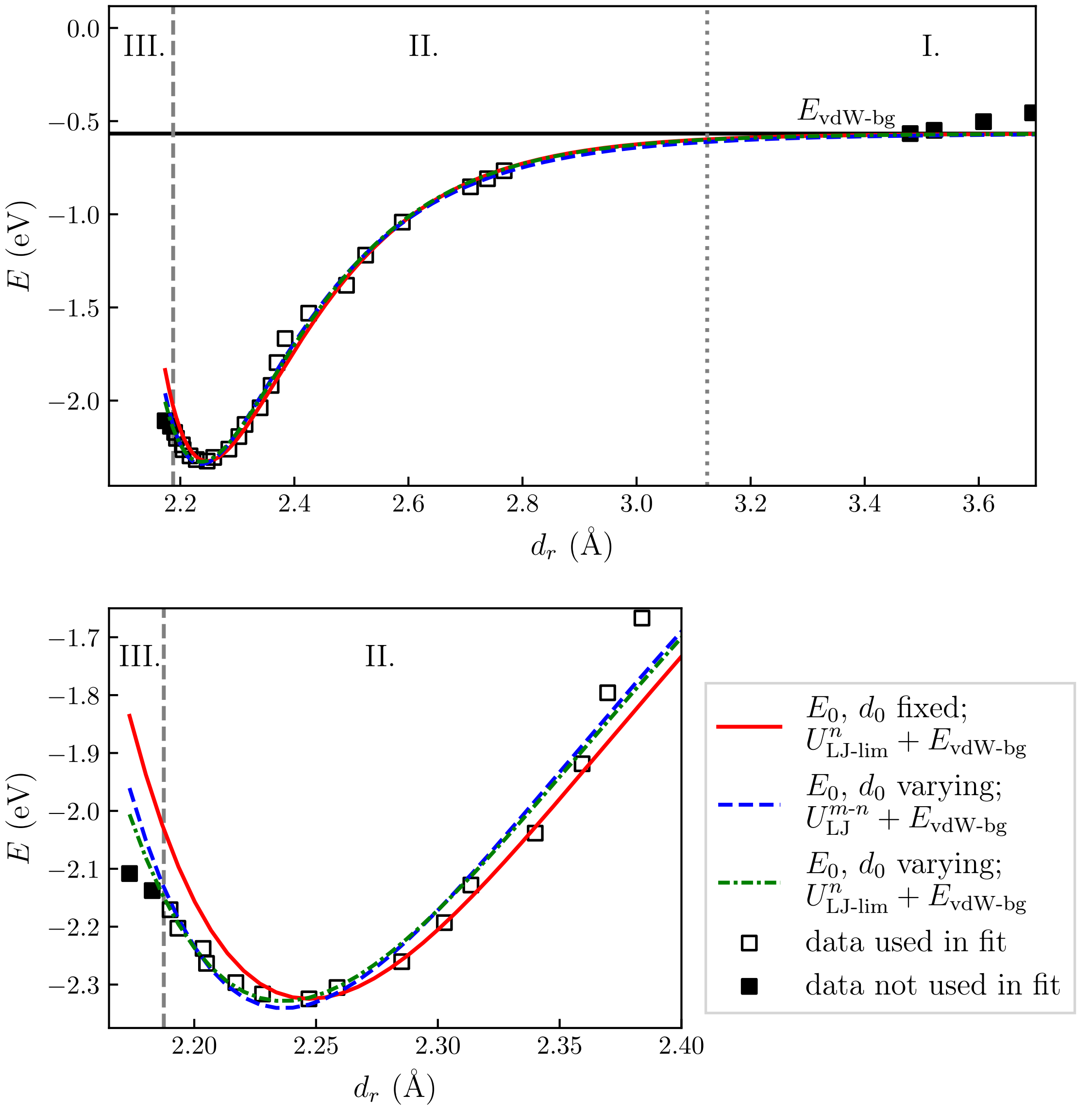

Fig. 5.10: Different fits to $E(d_r)$. The bottom panel shows the same thing as the top one, only zoomed in on the minimum to make differences between fits better visible. The fit using $U^{m\text{-}n}_{\text{LJ}}$ with fixed E_0, d_0 is not shown, but if it was it would lie perfectly on top of that where $U^n_{\text{LJ-lim}}$ was used.

5.4 Load dependence of the contact area

We now proceed to analyze the load dependence of the contact area. As stated previously, our analysis is restricted to the range of distances labeled II. in Figs. 5.6 and 5.10. We decided to parameterize $A(L)$ in terms of a general (i.e., with horizontal and vertical offset) power law

$$A_{\pm} = A_c \pm \alpha \cdot (L - L_c)^{\beta} \,, \tag{5.6}$$

where L_c is the pull-off force and A_c is the value of the contact area at $L = L_c$. The positive and negative signs distinguish the upper and lower branch of $A(L)$. One motivation for this Ansatz is that the predictions of common continuum models for $A(L)$ between a plane and a spherical asperity are either power laws (as in the Hertz and DMT models, with $\beta = 2/3$) or more general sublinear functions of L that, qualitatively, still resemble a power law (cf. Fig. 2.2). And while arguing on the basis of continuum models with regard to our atomistic simulation is of course questionable, our results for $A(L)$ also do not look too dissimilar from a power law. Another, practical, reason is that power-law fits are comparatively easy on a technical level. This is because, despite of the nonlinearity in the exponent parameter, one can conveniently determine α and β by means of a *linear* regression if one performs a logarithmic transform. To do so, we have to first rearrange and nondimensionalize Eq. 5.6, resulting in

$$\left| \frac{A_{\pm} - A_c}{A_{\mathrm{ref}}} \right| = \tilde{\alpha} \cdot \left(\frac{L - L_c}{L_{\mathrm{ref}}} \right)^{\beta} \,. \tag{5.7}$$

Here we have introduced some reference contact area A_{ref} and load L_{ref}, and a corresponding dimensionless prefactor $\tilde{\alpha} = (L_{\mathrm{ref}}^{\beta}/A_{\mathrm{ref}})\alpha$. Next, logarithmizing yields

$$\ln\left(\left| \frac{A_{\pm} - A_c}{A_{\mathrm{ref}}} \right| \right) = \beta \cdot \ln\left(\frac{L - L_c}{L_{\mathrm{ref}}} \right) + \ln(\tilde{\alpha}) \,, \tag{5.8}$$

from which β and $\ln(\tilde{\alpha})$ are estimated using linear regression. However, from this procedure we do not obtain the values of A_c and L_c. These need to be fixed before, so we take them directly from the point in our data with the minimum value of L. The reference values A_{ref} and L_{ref} can be chosen arbitrarily. Their only relevant effect on the fitting process is a vertical and/or horizontal shift of the data points in a log-log plot, reflected by the value of the intercept $\ln(\tilde{\alpha})$ in Eq. 5.8. Thus, to correctly reconstruct $A(L)$ from the regression coefficients β and $\ln(\tilde{\alpha})$, one needs to keep track of the values used for A_{ref} and L_{ref}, but they are otherwise unimportant. We simply set $A_{\mathrm{ref}} = 1\,\text{Å}^2$ and $L_{\mathrm{ref}} = 1\,\mathrm{nN}$.

At this point, it is appropriate to emphasize the difference in the analysis of $A(L)$ between Ref. [33] and our re-examination. In Ref. [33], certain functional forms for the description of $A(d_r)$ and $E(d_r)$ were chosen, from the combination of which $A \propto L^{1/2}$ followed (see Chap. 4 for details), without having to make any Ansatz for the functional form of $A(L)$. In this work, we start from a power-law Ansatz for $A(L)$, which in turn does not require an explicit expression for $A(d_r)$.

The upper branch $A_+(L)$ is the one most relevant for comparison with experiments, since only this branch of $A(L)$ is accessible in a load-control AFM setup (cf. the discussion in Sec. 2.1.2). In our simulations, however, this limitation does not apply. Therefore, for completeness, we did power-law fits to the upper and lower branch separately, as well as to both branches simultaneously. Note that in the fits to individual branches of $A(L)$, we nonetheless always use load values obtained from fitting to the *whole* region II. of the $E(d_r)$ curve, of which we then take only the subset of values corresponding to a particular branch of $A(L)$.

The load values used in this section for power-law fits to $A(L)$ were calculated from the parameterizations of $E(d_r)$ given by Tab. 5.2 and depicted in Fig. 5.10. We did this separately for both fit functions used to parameterize $E(d_r)$, i.e., $U_{\text{LJ}}^{m\text{-}n}(d_r)$ and $U_{\text{LJ-lim}}^{n}(d_r)$. If the whole procedure for calculating L from $E(d_r)$ and then analyzing $A(L)$ is robust, it should not make much of a difference to the final parameters characterizing $A(L)$ which parameterization for $E(d_r)$ was used. The resulting fit parameters for $A(L)$ are listed in Tab. 5.3. The coefficients of determination R^2 are also included as a measure of the goodness of fit of the linear regressions performed.[7]

Tab. 5.3: Parameters of power-law fits to $A(L)$ by logarithmic transform and linear regression. The coefficient $\tilde{\alpha}$ is defined as in Eq. 5.7 and reported here when $A_{\text{ref}} = 1\,\text{Å}^2$ and $L_{\text{ref}} = 1\,\text{nN}$.

loads computed from	branch of $A(L)$	β	$\tilde{\alpha}$	R^2
$U_{\text{LJ}}^{m\text{-}n}(d_r) + E_{\text{vdW-bg}}$	upper	0.44	3.67	0.94
	lower	0.51	2.59	0.99
	both	0.47	3.12	0.93
$U_{\text{LJ-lim}}^{n}(d_r) + E_{\text{vdW-bg}}$	upper	0.62	2.55	0.99
	lower	0.42	3.03	0.99
	both	0.52	2.94	0.96

To visualize the division of $A(L)$ into branches as well as the general shape of the curves, and to illustrate the procedure of fitting by logarithmic transform, the fit to

---

[7] Note that R^2 does not depend on the choice of A_{ref} and L_{ref}, as seen from the definition $R^2 = (\sum_{i=1}^{N}[\hat{f}(x_i) - \bar{y}]^2)/(\sum_{i=1}^{N}[y_i - \bar{y}]^2)$ [90], where y_i are the data points' dependent variable values, $\bar{y}$ their sample mean, and $\hat{f}(x_i)$ the model predictions at the independent variable values x_i. In our case, $y \mathrel{\widehat{=}} \ln((A - A_c)/A_{\text{ref}})$ and $x \mathrel{\widehat{=}} \ln((L - L_c)/L_{\text{ref}})$. Different choices of A_{ref} and L_{ref} only cause a vertical/horizontal shift of the data points, which cancels out in R^2.

$A(L)$ is shown in Fig. 5.11 for the case of L computed from $U^{n}_{\text{LJ-lim}}(d_r)$. The power-law parameters corresponding to the fit curves plotted in that figure are those in the bottom half of Tab. 5.3. The resulting curves when using the loads calculated from $U^{m\text{-}n}_{\text{LJ}}(d_r)$ (not shown) are qualitatively similar. The power-law fit is seen to be not perfect, but we believe it is acceptable for the purpose of simply finding a reasonable description of $A(L)$ in terms of a small number of parameters.

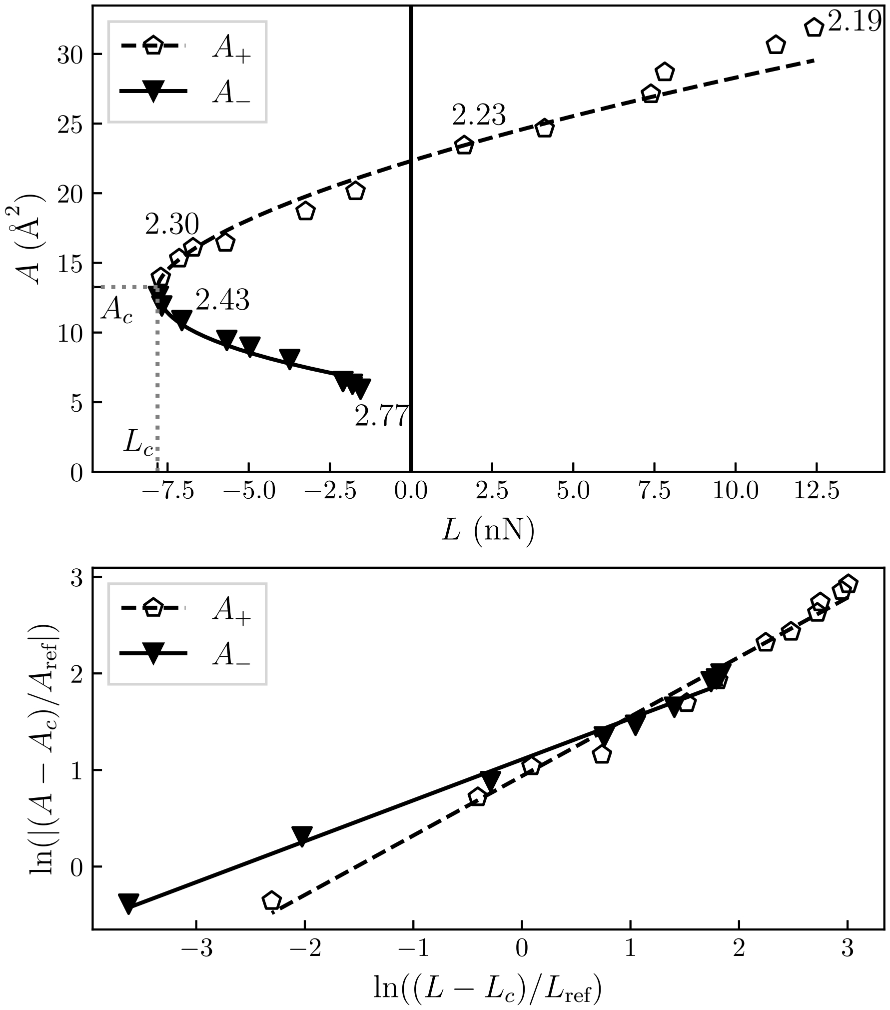

Fig. 5.11: Power-law fits to different branches of $A(L)$. The fit to both branches simultaneously (not shown) would consist of a straight-line fit to the union of the A_+ and A_- data points in the log-log plot. The numbers in the upper panel are the corresponding values of some distances d_r in Å.

As seen in Tab. 5.3, the loads calculated from $U^{m\text{-}n}_{\text{LJ}}(d_r)$ and $U^{n}_{\text{LJ-lim}}(d_r)$ do not lead to quite the same exponents for $A(L)$. For the experimentally most relevant upper branch of $A(L)$, the former gives β closer to 2/5, the latter closer to 3/5. Similarly, for the lower branch there is also a difference, though a smaller one. Based on R^2 as a criterion, the power-law description of $A(L)$ is also slightly worse when using the loads calculated from $U_{\text{LJ}}^{m\text{-}n}(d_r)$. Since the parameterizations of $E(d_r)$ with $U_{\text{LJ}}^{m\text{-}n}(d_r)$ and $U_{\text{LJ-lim}}^{n}(d_r)$ are visually quite similar and by all means both look reasonable (cf. Fig. 5.10), we have to conclude that the power-law fits to $A(L)$ are rather sensitive to the specific method by which the load is calculated from the tip-surface interaction energy. However, this difference between $U_{\text{LJ}}^{m\text{-}n}(d_r)$ and $U_{\text{LJ-lim}}^{n}(d_r)$ in the exponents found for $A(L)$ is present only when looking at the individual branches of $A(L)$ alone. The simultaneous fits to both branches of $A(L)$ give values of β close to 1/2 for both $U_{\text{LJ}}^{m\text{-}n}(d_r)$ and $U_{\text{LJ-lim}}^{n}(d_r)$. It therefore appears that the A-vs-L fits are more robust to slight differences in the load calculation when the entire curve (i.e., both the upper and lower branch) is considered at once.

While the exponent value of about 1/2 for $A(L)$ does in fact agree with the original study by Wolloch *et al.* [33], this may be only a coincidence and not lend itself to direct comparison. The reason is that the regions used in fitting are different. In the present work, we obtained $\beta \approx 1/2$ when considering the entire upper and lower branches of $A(L)$ at the same time. In the past study, by contrast, it was obtained for a vicinity of the minimum of $E(d_r)$, which in the A-vs-L curve corresponds to a region around $L = 0$ within the upper branch.

5.4.1 Interpretation in terms of a continuum model

Finally, we briefly compare our *ab-initio* results with continuum predictions. It is, *a priori*, not clear that continuum models should be applicable at all in our case, given that we are dealing with an atomically sharp tip and contact dimensions of Ångström scale. That would make it noteworthy if we find that our results are nonetheless consistent with a continuum description. In this context, we also point out two studies by Lee *et al.* [91, 92], in which finite-element simulations were successfully used to interpret AFM nanoindetation and nanofriction experiments on graphene. While these studies are not immediately related to the question of the load-dependent contact area that we investigate in this thesis, they show that a continuum description of nanotribological properties of graphene is at least not without precedent.

For a comparison of our results with continuum models, we will focus on the Thin-Coating Contact Mechanics (TCCM) model by Reedy [44], introduced earlier in Sec. 2.1.3. The graphene layer in our system corresponds to the elastic coating in that model. Even though not all of TCCM's assumptions are perfectly fulfilled or even conceptually strictly applicable in our system, it is probably still the closest analog as far as available continuum models go:

- TCCM assumes both a rigid substrate and rigid indenter. The former assumption clearly matches the conditions in our simulations, since we hold the iridium substrate fixed. The latter is also approximately true since most of the deformation occurs in the graphene rather than in the tip (cf. Fig. 5.1b).
- The assumption $h/R \ll 1$ of the coating thickness h being much less than the indenter radius R is slightly more questionable for our system. The exact values to be assigned to h and R are of course a matter of debate. If, e.g., one takes the coating thickness to be the height of the carbon atoms in the undeformed graphene layer above the iridium substrate, then $h \approx 3.42\,\text{Å}$. As for the radius R of the tip, it is not perfectly well-defined since the tip in our system is not actually truly spherical. However, regardless of the exact values, it can probably not be argued that $R \gg h$ is perfectly fulfilled, considering the sharpness of the tip.
- In a similar vein, the assumption $a/h \gg 1$ of the contact radius a being much larger than the coating thickness h is also arguably not fulfilled. The lateral dimensions of the contact regions are only a few Ångströms (cf. Fig. 5.5), and thus of comparable size to the coating thickness h (if one uses again $h \approx 3.42\,\text{Å}$).
- TCCM was developed and numerically validated only for values of Poisson's ratio $\nu < 0.45$. If one takes the Poisson's ratio of graphene to be that of graphite in the basal plane, i.e., $\nu = 0.165$, as was done in the finite-element simulations of graphene in Ref. [91], this requirement is comfortably fulfilled.
- We did not specifically investigate whether the assumption of deformations within the linear elastic regime is satisfied.

For the separate branches of $A(L)$ on their own, a reliable continuum interpretation of our results does not seem to be possible. After all, the differences in β between fits where L is taken from different parameterizations of $E(d_r)$ (cf. Tab. 5.3) are comparable to the differences in the exponents between some continuum models (Hertz- or DMT-like contacts with $\beta = 2/3$, TCCM with $\beta = 1/2$). So, we would find it hard to reliably distinguish between different continuum models based on these data. But when fitting to the whole $A(L)$ curve, where our exponents are approximately the same regardless of the parameterization used for $E(d_r)$, we argue that they are more reliable. For this case, the value of β close to $1/2$ that we found does in fact agree with TCCM.

6 Conclusions and outlook

Building upon previous work on the same question and system by Wolloch *et al.* [33], we studied the load dependence of the atomic-scale real contact area between a tungsten AFM tip and a graphene layer on iridium, using an *ab-initio* contact model. We extended, and deviated from, the past analysis in two main ways. Firstly, we ran calculations at a more finely-spaced set of tip-sample separations. Secondly, we used different fitting strategies and model functions for calculating the load from the tip-surface interaction potential and extracting the load dependence of the contact area.

To calculate the loads from the interaction potential $E(d_r)$ as a function of the relaxed tip-sample distance d_r, we initially sought a single analytic parameterization of $E(d_r)$ that works for all distances d_r. But we found this to be impractical, given that $E(d_r)$ comprises several distinct interaction regimes at different separation ranges. So we focused only on a certain range below the 'jump-to-contact' between tip and sample, where a description of $E(d_r)$ with a generalized Lennard-Jones potential (with variable exponents m and n) seemed applicable. Attempts to give a physical interpretation to the values obtained for the Lennard-Jones fit parameters m and n unfortunately remained largely unsatisfactory. So we treated this parameterization of $E(d_r)$ as mostly just a tool for load calculation.

As for the central question of the load-dependent real contact area, we observed that a power-law parameterization of $A(L)$ displays some sensitivity to the specific way the loads are computed from the energy-distance curve, when only individual branches of $A(L)$ are considered at a time. Further investigations of this apparent sensitivity might be advisable in the future. When, however, the whole curve $A(L)$ accessible to our simulations is considered at once, the parameterizations of $A(L)$ appear more robust and we therefore have confidence in them. For the latter case, we find an exponent close to $1/2$ in a power-law description of $A(L)$. This agrees with Reedy's Thin-Coating Contact Mechanics, a model that we argued is the closest equivalent to our system in terms of continuum models. Our results thus give some tentative validation to the practice of applying continuum contact models on atomic scales.

Although the exponent value of about $\approx 1/2$ that we found matches the original result from Ref. [33], we argued that our result is not entirely comparable to this past study, as the region of the A-vs-L curve for which it was obtained is different. However, rather than being a limitation, this is by design, since it was our intention from the start to capture $A(L)$ across a greater range of values of L than in the original study.

Ultimately, conclusive tests of our results and the *ab-initio* contact model in general will have to come from comparison with friction-vs-load curves, either from other simulations or from experiments. For better comparability in possible future tests of the model, one may use systems with simpler tip-sample interaction potentials, since the range of distances that can be (easily) investigated is limited in the case at hand by the interaction becoming again attractive at small distances due to tip-sample bonding. Another interesting avenue for future extension of the computational model might be coupling of the tip to a more realistic, flexible AFM cantilever.

Acknowledgements

This work was funded by the "Austrian COMET-Program" (project InTribology, no. 872176) via the Austrian Research Promotion Agency (FFG) and the Provinces of Niederösterreich and Vorarlberg and has been carried out within the “Excellence Centre of Tribology” (AC2T research GmbH).

The computational results presented have been partially obtained at the Vienna Scientific Cluster (VSC).

First and foremost, I would like to thank my supervisors, Prof. András Vernes and Prof. Markus Valtiner who found the time for many productive discussions and supported and guided me through this work. I am indebted to them for giving me the opportunity to become acquainted with the field of tribology — not a field that had featured heavily in my studies up to this point, despite its significance — and to gain experience in first-principles atomistic modeling. The things and skills I learned in the process will undoubtedly prove valuable to me in the future. And of course I cannot close without expressing my gratitude to Michael Wolloch, without the groundwork of whom the present work would not have been possible, and who was always extremely quick and helpful in answering me when I had some questions to him.

I also want to thank my former colleagues at AC2T research who made for enjoyable lunch and coffee breaks. Finally, I appreciate the efforts of all those who worked tirelessly to keep things running as smoothly as possible when the COVID-19 pandemic hit halfway through my thesis and complicated working and communicating.

A Detailed results

Tab. A.1 shows details on the relaxations for each distance. As in the rest of this thesis, d_r is to be understood as referring to the z component of the length that connects the tip apex and the carbon atom most directly below: $d_r \equiv d_{r,z}$. The lateral component $d_{r,lat}$ (component that lies in the x-y plane) is included alongside it. The energies reported are relative to that at the largest distance included.

Information on the initial configuration, or sequence of initial configurations, used in the relaxation of each distance is also included. The notation used for this is best explained by means of an example. Consider the tip position labeled $d_s = 1.09$ Å, with initial configuration labeled in Tab. A.1 as '1.40 ← static'. By this, we mean that we first created a static configuration ('static' as defined in Sec. 3.2) with $d_s = 1.40$ Å, and relaxed it. In the resulting relaxed configuration, the tip was then translated downward by 0.21 Å to create the initial configuration from which the tip position labeled $d_s = 1.09$ Å was finally relaxed.

Tab. A.2 shows the contact areas A and numbers N_e^{vac} of electrons assigned to the vacuum region, for two different electron density cutoffs. The lower cutoff, 5.0×10^{-2} electrons/Å^3, is what was used in Ref. [33]. The higher one is our slightly revised value, for consistency with our additional data. Only distances up to the first distance above the jump-to-contact are included, for all larger distances the contact areas were not explicitly calculated as they are zero by construction.

Tab. A.1: Details on relaxation for each distance. See text at beginning of this chapter for more explanation.

d_s (Å)	sequence of initial configurations	d_r (Å)	$d_{r,lateral}$ (Å)	E (eV)
1.09	1.40 ← static	2.17	0.05	-2.11
1.20	1.40 ← static	2.18	0.05	-2.14
1.30	1.40 ← static	2.19	0.03	-2.17
1.40	static	2.19	0.05	-2.20
1.46	1.40 ← static	2.20	0.05	-2.24
1.51	2.29 ← static	2.21	0.04	-2.26
1.60	2.29 ← static	2.22	0.04	-2.30
1.68	2.29 ← static	2.23	0.04	-2.32
1.85	2.29 ← static	2.25	0.03	-2.32
2.00	2.29 ← static	2.26	0.03	-2.31
2.18	2.29 ← static	2.29	0.02	-2.26
2.29	2.66 ← 3.14 ← static	2.30	0.03	-2.19
2.40	2.66 ← 3.14 ← static	2.31	0.04	-2.13
2.53	2.29 ← static	2.34	0.03	-2.04
2.66	3.14 ← static	2.36	0.03	-1.92
2.78	3.14 ← static	2.37	0.03	-1.80
2.90	3.14 ← static	2.38	0.03	-1.67
3.02	3.14 ← static	2.43	0.02	-1.53
3.14	static	2.49	0.02	-1.38
3.27	3.14 ← static	2.52	0.02	-1.22
3.40	3.53 ← static	2.59	0.03	-1.04
3.53	static	2.71	0.03	-0.85
3.56	3.53 ← static	2.74	0.03	-0.81
3.59	3.53 ← static	2.77	0.03	-0.77
3.63	3.65 ← static	3.48	0.00	-0.57
3.65	static	3.52	0.00	-0.55
3.71	static	3.61	0.00	-0.50
3.78	static	3.69	0.00	-0.46
3.85	static	3.78	0.00	-0.41
3.97	static	3.92	0.00	-0.34
4.07	static	4.03	0.00	-0.29
4.17	static	4.14	0.00	-0.25
4.28	static	4.25	0.00	-0.21
4.40	static	4.39	0.00	-0.16
4.60	static	4.59	0.00	-0.11
4.79	static	4.78	0.00	-0.07
4.98	static	4.98	0.00	-0.04
5.16	static	5.16	0.00	-0.02
5.34	static	5.34	0.00	-0.01
5.51	static	5.51	0.00	0.00

Tab. A.2: Contact areas A and vacuum charges at different distances. See text at beginning of this chapter for more explanation.

		vacuum density cutoff (electrons/Å^3)			
		5.25×10^{-2}		5.0×10^{-2}	
d_s (Å)	d_r (Å)	A (Å^2)	N_e^{vac}	A (Å^2)	N_e^{vac}
1.09	2.17	38.36	30.51	39.86	28.21
1.20	2.18	34.88	30.65	36.41	28.34
1.30	2.19	31.88	30.82	33.49	28.49
1.40	2.19	30.64	30.73	31.76	28.35
1.46	2.20	28.69	30.81	29.62	28.44
1.51	2.21	27.11	31.03	28.44	28.65
1.60	2.22	24.65	31.13	26.03	28.73
1.68	2.23	23.43	31.21	24.11	28.81
1.85	2.25	20.15	31.38	21.02	28.96
2.00	2.26	18.70	31.60	19.70	29.12
2.18	2.29	16.45	31.83	17.14	29.32
2.29	2.30	16.09	32.48	16.75	29.99
2.40	2.31	15.31	32.65	15.94	30.18
2.53	2.34	13.96	32.69	14.70	30.21
2.66	2.36	13.26	33.15	13.88	30.67
2.78	2.37	12.59	33.24	13.29	30.77
2.90	2.38	11.90	33.28	12.60	30.82
3.02	2.43	10.85	33.30	11.49	30.84
3.14	2.49	9.43	33.34	10.10	30.88
3.27	2.52	8.94	33.54	9.34	31.08
3.40	2.59	8.06	33.62	8.68	31.17
3.53	2.71	6.48	33.68	6.95	31.23
3.56	2.74	6.28	33.69	6.63	31.24
3.59	2.77	5.93	33.71	6.41	31.26
3.63	3.48	0.00	32.41	0.25	29.87

B Limit of m-n Lennard-Jones potential as $m \to n$

We want to calculate the limit $m \to n$ of the m-n Lennard-Jones potential, with depth E_0 and equilibrium distance d_0 fixed,

$$U_{\mathrm{LJ}}^{m\text{-}n}(d_r) = -\frac{E_0}{m-n}\left[m\left(\frac{d_0}{d_r}\right)^n - n\left(\frac{d_0}{d_r}\right)^m\right], \tag{B.1}$$

$$U_{\text{LJ-lim}}^{n}(d_r) \coloneqq \lim_{m\to n} U_{\mathrm{LJ}}^{m\text{-}n}(d_r)\,. \tag{B.2}$$

First, we define the abbreviation $s \coloneqq d_0/d_r$. Next, let us calculate the limit of the relevant parts containing m and n (omitting the prefactor $-E_0$ for brevity):

$$\begin{aligned}
\lim_{m\to n}\frac{ms^n - ns^m}{m-n} &= \frac{\text{‘}0\text{’}}{0} \\
&= \lim_{m\to n}\frac{\frac{d}{dm}[ms^n - ns^m]}{\frac{d}{dm}[m-n]} \\
&= \lim_{m\to n}\frac{s^n - n\frac{d}{dm}s^m}{1} \\
&= \lim_{m\to n}[s^n - n\ln(s)s^m] \\
&= s^n - n\ln(s)s^n \\
&= [1 - n\ln(s)]\cdot s^n
\end{aligned} \tag{B.3}$$

In passing from the first to the second line, L’Hôpital’s rule was used to deal with what would be an undefined expression when applying the limit to numerator and denominator separately.

Finally, adding back in the prefactor and plugging in the definition of s, we obtain

$$U_{\text{LJ-lim}}^{n}(d_r) = -E_0\cdot\left[1 - n\ln\left(\frac{d_0}{d_r}\right)\right]\cdot\left(\frac{d_0}{d_r}\right)^n. \tag{B.4}$$

For the derivative of this w.r.t. the distance, we find

$$\frac{\partial}{\partial d_r} U^{n}_{\text{LJ-lim}}(d_r) = -\frac{E_0}{d_0} n^2 \ln\left(\frac{d_0}{d_r}\right) \cdot \left(\frac{d_0}{d_r}\right)^{n+1} . \tag{B.5}$$

C Lennard-Jones fit details

Our fits to $E(d_r)$ were done by standard nonlinear least-squares fitting, i.e., by minimization of the quantity chi-square, written generically as

$$\chi^2(\boldsymbol{\theta}) = \sum_{i=1}^{N} \frac{[f(x_i;\boldsymbol{\theta}) - y_i]^2}{\sigma_i^2} \,. \tag{C.1}$$

In this expression, the x_i denote the ith value of the independent variable out of N data points, and the y_i that of the dependent variable. The σ_i are the uncertainties (standard deviations) in the data y_i. The model function, with P fitting parameters $\boldsymbol{\theta} = (\theta_1, \ldots, \theta_P)$, evaluated at x_i, is denoted by $f(x_i;\boldsymbol{\theta})$.

The optimal fit parameters $\boldsymbol{\theta}_{\text{opt}}$ are then obtained as those minimizing Eq. C.1,

$$\boldsymbol{\theta}_{\text{opt}} = \arg\min_{\boldsymbol{\theta}} \chi^2(\boldsymbol{\theta}) \,. \tag{C.2}$$

The *lmfit* package [73] that we used for this by default employs a Levenberg–Marquardt algorithm [93, 94] to perform the required nonlinear minimization.

In our case, the x_i correspond to the relaxed distance d_r, the y_i to the energy E, and the model function f is the m-n Lennard-Jones potential, either in the 'standard' version $U_{\text{LJ}}^{m\text{-}n}(d_r)$ (Eq. 5.1) or the 'limit' version $U_{\text{LJ-lim}}^{n}(d_r)$ (Eq. 5.5). The fitting parameters $\boldsymbol{\theta}$ correspond to (m, n, E_0, d_0) in the case of $U_{\text{LJ}}^{m\text{-}n}$, or (n, E_0, d_0) in the case of $U_{\text{LJ-lim}}^{n}$.

In the situation of Gaussian noise with zero mean in the data, the minimization of $\chi^2(\boldsymbol{\theta})$ possesses an interpretation as a maximum-likelihood estimate of the parameters [95], since in this case χ^2 is related to the so-called log-likelihood function $\ln\mathcal{L}$ by

$$-\ln\mathcal{L}(\boldsymbol{\theta}) = \frac{1}{2}\chi^2(\boldsymbol{\theta}) \,. \tag{C.3}$$

In our case, however, the data uncertainties are not truly of statistical nature, since our simulations results are in principle deterministic[8]. So we simply and

---

[8] We believe there are some uncertainties in the data that appear random from a user's perspective, namely due to possibly imperfect ionic relaxations, but whether these qualify as Gaussian noise is a matter of debate.

pragmatically view χ^2 as mostly a convenient measure of the geometric deviation of the model function from the data. For that purpose, the σ_i are treated simply as weights, that we all set to one.

List of Figures

List of Tables

Bibliography

[1] Kenneth Langstreth Johnson. *Contact Mechanics.* en. Cambridge University Press, Aug. 1987. ISBN: 978-0-521-34796-9.

[2] Ian M. Hutchings. "Leonardo Da Vinci's Studies of Friction". en. In: *Wear* 360-361 (Aug. 2016), pp. 51–66. ISSN: 0043-1648. DOI: `10.1016/j.wear.2016.04.019`.

[3] Guillaume Amontons. "De la resistance causée dans les machines". fr. In: *Histoire de l'Académie royale des sciences ... avec les mémoires de mathématique & de physique* (1699). Ed. by Académie des sciences (France), pp. 206–227.

[4] Charles Augustin de Coulomb. "Théorie des machines simples". fr. In: *Mémoires de mathématique et de physique* 10 (1785), pp. 161–332.

[5] Frank Philip Bowden and David Tabor. "The Area of Contact between Stationary and Moving Surfaces". In: *Proceedings of the Royal Society of London. Series A. Mathematical and Physical Sciences* 169.938 (Feb. 1939), pp. 391–413. DOI: `10.1098/rspa.1939.0005`.

[6] F. P. Bowden and D. Tabor. "Mechanism of Metallic Friction". en. In: *Nature* 150.3798 (Aug. 1942), pp. 197–199. ISSN: 1476-4687. DOI: `10.1038/150197a0`.

[7] J. F. Archard. "Elastic Deformation and the Laws of Friction". In: *Proceedings of the Royal Society of London. Series A. Mathematical and Physical Sciences* 243.1233 (Dec. 1957), pp. 190–205. DOI: `10.1098/rspa.1957.0214`.

[8] J. A. Greenwood and J. B. P. Williamson. "Contact of Nominally Flat Surfaces". In: *Proceedings of the Royal Society of London. Series A. Mathematical and Physical Sciences* 295.1442 (Dec. 1966), pp. 300–319. DOI: `10.1098/rspa.1966.0242`.

[9] Izabela Szlufarska, Michael Chandross, and Robert W. Carpick. "Recent Advances in Single-Asperity Nanotribology". en. In: *Journal of Physics D: Applied Physics* 41.12 (May 2008), p. 123001. ISSN: 0022-3727. DOI: `10.1088/0022-3727/41/12/123001`.

[10] Robert W. Carpick and Miquel Salmeron. "Scratching the Surface: Fundamental Investigations of Tribology with Atomic Force Microscopy". In: *Chemical Reviews* 97.4 (June 1997), pp. 1163–1194. ISSN: 0009-2665. DOI: `10.1021/cr960068q`.

[11] Roland Bennewitz. "Friction Force Microscopy". en. In: *Materials Today* 8.5 (May 2005), pp. 42–48. ISSN: 1369-7021. DOI: `10.1016/S1369-7021(05)00845-X`.

[12] R. W. Carpick et al. "Measurement of Interfacial Shear (Friction) with an Ultrahigh Vacuum Atomic Force Microscope". In: *Journal of Vacuum Science & Technology B: Microelectronics and Nanometer Structures Processing, Measurement, and Phenomena* 14.2 (Mar. 1996), pp. 1289–1295. ISSN: 1071-1023. DOI: `10.1116/1.589083`.

[13] R. W. Carpick et al. "Variation of the Interfacial Shear Strength and Adhesion of a Nanometer-Sized Contact". In: *Langmuir* 12.13 (Jan. 1996), pp. 3334–3340. ISSN: 0743-7463. DOI: `10.1021/la9509007`.

[14] R. W. Carpick, D. F. Ogletree, and M. Salmeron. "Lateral Stiffness: A New Nanomechanical Measurement for the Determination of Shear Strengths with Friction Force Microscopy". In: *Applied Physics Letters* 70.12 (Mar. 1997), pp. 1548–1550. ISSN: 0003-6951. DOI: `10.1063/1.118639`.

[15] Udo D. Schwarz et al. "Quantitative Analysis of the Frictional Properties of Solid Materials at Low Loads. I. Carbon Compounds". In: *Physical Review B* 56.11 (Sept. 1997), pp. 6987–6996. DOI: `10.1103/PhysRevB.56.6987`.

[16] R. W. Carpick et al. "Making, Breaking and Sliding of Nanometer-Scale Contacts". en. In: *MRS Online Proceedings Library Archive* 539 (1998/ed). ISSN: 0272-9172, 1946-4274. DOI: `10.1557/PROC-539-93`.

[17] M. Enachescu et al. "Observation of Proportionality between Friction and Contact Area at the Nanometer Scale". en. In: *Tribology Letters* 7.2 (Sept. 1999), p. 73. ISSN: 1573-2711. DOI: `10.1023/A:1019173404538`.

[18] E. Riedo et al. "Nanotribology of Carbon Based Thin Films: The Influence of Film Structure and Surface Morphology". en. In: *Surface Science* 477.1 (Apr. 2001), pp. 25–34. ISSN: 0039-6028. DOI: `10.1016/S0039-6028(01)00701-4`.

[19] M. A. Lantz, S. J. O'Shea, and M. E. Welland. "Simultaneous Force and Conduction Measurements in Atomic Force Microscopy". In: *Physical Review B* 56.23 (Dec. 1997), pp. 15345–15352. DOI: `10.1103/PhysRevB.56.15345`.

[20] Binquan Luan and Mark O. Robbins. "The Breakdown of Continuum Models for Mechanical Contacts". en. In: *Nature* 435.7044 (June 2005), pp. 929–932. ISSN: 1476-4687. DOI: `10.1038/nature03700`.

[21] Binquan Luan and Mark O. Robbins. "Contact of Single Asperities with Varying Adhesion: Comparing Continuum Mechanics to Atomistic Simulations". In: *Physical Review E* 74.2 (Aug. 2006), p. 026111. DOI: `10.1103/PhysRevE.74.026111`.

[22] Shengfeng Cheng and Mark O. Robbins. “Defining Contact at the Atomic Scale”. en. In: *Tribology Letters* 39.3 (Sept. 2010), pp. 329–348. ISSN: 1573-2711. DOI: 10.1007/s11249-010-9682-5.

[23] Soheil Solhjoo and Antonis I. Vakis. “Single Asperity Nanocontacts: Comparison between Molecular Dynamics Simulations and Continuum Mechanics Models”. en. In: *Computational Materials Science* 99 (Mar. 2015), pp. 209–220. ISSN: 0927-0256. DOI: 10.1016/j.commatsci.2014.12.010.

[24] Soheil Solhjoo and Antonis I. Vakis. “Definition and Detection of Contact in Atomistic Simulations”. en. In: *Computational Materials Science* 109 (Nov. 2015), pp. 172–182. ISSN: 0927-0256. DOI: 10.1016/j.commatsci.2015.07.026.

[25] Soheil Solhjoo and Antonis I. Vakis. “Continuum Mechanics at the Atomic Scale: Insights into Non-Adhesive Contacts Using Molecular Dynamics Simulations”. In: *Journal of Applied Physics* 120.21 (Dec. 2016), p. 215102. ISSN: 0021-8979. DOI: 10.1063/1.4967795.

[26] Yifei Mo, Kevin T. Turner, and Izabela Szlufarska. “Friction Laws at the Nanoscale”. en. In: *Nature* 457.7233 (Feb. 2009), pp. 1116–1119. ISSN: 1476-4687. DOI: 10.1038/nature07748.

[27] Yifei Mo and Izabela Szlufarska. “Roughness Picture of Friction in Dry Nanoscale Contacts”. In: *Physical Review B* 81.3 (Jan. 2010), p. 035405. DOI: 10.1103/PhysRevB.81.035405.

[28] S. Eder et al. “Molecular Dynamics Simulations of Mixed Lubrication with Smooth Particle Post-Processing”. en. In: *Journal of Physics: Condensed Matter* 23.17 (Apr. 2011), p. 175004. ISSN: 0953-8984. DOI: 10.1088/0953-8984/23/17/175004.

[29] András Vernes et al. “On the Three-Term Kinetic Friction Law in Nanotribological Systems”. en. In: *Faraday Discussions* 156.0 (July 2012), pp. 173–196. ISSN: 1364-5498. DOI: 10.1039/C2FD00120A.

[30] Stefan J. Eder, András Vernes, and Gerhard Betz. “On the Derjaguin Offset in Boundary-Lubricated Nanotribological Systems”. In: *Langmuir* 29.45 (Nov. 2013), pp. 13760–13772. ISSN: 0743-7463. DOI: 10.1021/la4026443.

[31] S. Eder, A. Vernes, and G. Betz. “Methods and Numerical Aspects of Nanoscopic Contact Area Estimation in Atomistic Tribological Simulations”. en. In: *Computer Physics Communications* 185.1 (Jan. 2014), pp. 217–228. ISSN: 0010-4655. DOI: 10.1016/j.cpc.2013.09.021.

[32] S. J. Eder et al. “Applicability of Macroscopic Wear and Friction Laws on the Atomic Length Scale”. In: *Physical Review Letters* 115.2 (2015), p. 025502. DOI: 10.1103/PhysRevLett.115.025502.

[33] M. Wolloch et al. “Ab Initio Calculation of the Real Contact Area on the Atomic Scale”. In: *Physical Review B* 91.19 (May 2015), p. 195436. DOI: `10.1103/PhysRevB.91.195436`.

[34] Richard F. W. Bader. *Atoms in Molecules: A Quantum Theory*. en. Clarendon Press, 1990. ISBN: 978-0-19-855168-3.

[35] Heinrich Hertz. “Ueber die Berührung fester elastischer Körper.” de. In: *Journal für die reine und angewandte Mathematik* 92 (1882), pp. 156–171. ISSN: 0075-4102.

[36] Kenneth Langstreth Johnson, Kevin Kendall, and A. D. Roberts. “Surface Energy and the Contact of Elastic Solids”. In: *Proceedings of the Royal Society of London. A. Mathematical and Physical Sciences* 324.1558 (Sept. 1971), pp. 301–313. DOI: `10.1098/rspa.1971.0141`.

[37] Michelle L. Oyen. *Handbook of Nanoindentation: With Biological Applications*. en. CRC Press, Apr. 2019. ISBN: 978-981-4241-60-1.

[38] B. V Derjaguin, V. M Muller, and Yu. P Toporov. “Effect of Contact Deformations on the Adhesion of Particles”. en. In: *Journal of Colloid and Interface Science* 53.2 (Nov. 1975), pp. 314–326. ISSN: 0021-9797. DOI: `10.1016/0021-9797(75)90018-1`.

[39] Daniel Maugis. “Adhesion of Spheres: The JKR-DMT Transition Using a Dugdale Model”. en. In: *Journal of Colloid and Interface Science* 150.1 (Apr. 1992), pp. 243–269. ISSN: 0021-9797. DOI: `10.1016/0021-9797(92)90285-T`.

[40] D Tabor. “Surface Forces and Surface Interactions”. en. In: *Journal of Colloid and Interface Science*. International Conference on Colloids and Surfaces 58.1 (Jan. 1977), pp. 2–13. ISSN: 0021-9797. DOI: `10.1016/0021-9797(77)90366-6`.

[41] J. A. Greenwood. “Adhesion of Elastic Spheres”. In: *Proceedings of the Royal Society of London. Series A: Mathematical, Physical and Engineering Sciences* 453.1961 (June 1997), pp. 1277–1297. DOI: `10.1098/rspa.1997.0070`.

[42] Robert W. Carpick, D. Frank Ogletree, and Miquel Salmeron. “A General Equation for Fitting Contact Area and Friction vs Load Measurements”. en. In: *Journal of Colloid and Interface Science* 211.2 (Mar. 1999), pp. 395–400. ISSN: 0021-9797. DOI: `10.1006/jcis.1998.6027`.

[43] Etienne Barthel. “On the Description of the Adhesive Contact of Spheres with Arbitrary Interaction Potentials”. en. In: *Journal of Colloid and Interface Science* 200.1 (Apr. 1998), pp. 7–18. ISSN: 0021-9797. DOI: `10.1006/jcis.1997.5309`.

[44] E. D. Reedy. "Thin-Coating Contact Mechanics with Adhesion". en. In: *Journal of Materials Research* 21.10 (Oct. 2006), pp. 2660–2668. ISSN: 2044-5326, 0884-2914. DOI: 10.1557/jmr.2006.0327.

[45] Gerd Czycholl. *Theoretische Festkörperphysik: Von den klassischen Modellen zu modernen Forschungsthemen*. de. Third. Springer-Lehrbuch. Berlin Heidelberg: Springer-Verlag, 2008. ISBN: 978-3-540-74790-1. DOI: 10.1007/978-3-540-74790-1.

[46] Klaus Capelle. "A Bird's-Eye View of Density-Functional Theory". en. In: *Brazilian Journal of Physics* 36.4A (Dec. 2006), pp. 1318–1343. ISSN: 0103-9733. DOI: 10.1590/S0103-97332006000700035.

[47] M. Born and R. Oppenheimer. "Zur Quantentheorie der Molekeln". de. In: *Annalen der Physik* 389.20 (1927), pp. 457–484. ISSN: 1521-3889. DOI: 10.1002/andp.19273892002.

[48] P. Hohenberg and W. Kohn. "Inhomogeneous Electron Gas". In: *Physical Review* 136.3B (Nov. 1964), B864–B871. DOI: 10.1103/PhysRev.136.B864.

[49] D. R. Hartree. "The Wave Mechanics of an Atom with a Non-Coulomb Central Field. Part I. Theory and Methods". en. In: *Mathematical Proceedings of the Cambridge Philosophical Society* 24.1 (Jan. 1928), pp. 89–110. ISSN: 1469-8064, 0305-0041. DOI: 10.1017/S0305004100011919.

[50] W. Kohn and L. J. Sham. "Self-Consistent Equations Including Exchange and Correlation Effects". In: *Physical Review* 140.4A (Nov. 1965), A1133–A1138. DOI: 10.1103/PhysRev.140.A1133.

[51] Stefan Grimme et al. "Dispersion-Corrected Mean-Field Electronic Structure Methods". In: *Chemical Reviews* 116.9 (May 2016), pp. 5105–5154. ISSN: 0009-2665. DOI: 10.1021/acs.chemrev.5b00533.

[52] M. Dion et al. "Van Der Waals Density Functional for General Geometries". In: *Physical Review Letters* 92.24 (June 2004), p. 246401. DOI: 10.1103/PhysRevLett.92.246401.

[53] Guillermo Román-Pérez and José M. Soler. "Efficient Implementation of a van Der Waals Density Functional: Application to Double-Wall Carbon Nanotubes". In: *Physical Review Letters* 103.9 (Aug. 2009), p. 096102. DOI: 10.1103/PhysRevLett.103.096102.

[54] Jiří Klimeš, David R. Bowler, and Angelos Michaelides. "Van Der Waals Density Functionals Applied to Solids". In: *Physical Review B* 83.19 (May 2011), p. 195131. DOI: 10.1103/PhysRevB.83.195131.

[55] R. P. Feynman. "Forces in Molecules". In: *Physical Review* 56.4 (Aug. 1939), pp. 340–343. DOI: 10.1103/PhysRev.56.340.

[56] Richard F. W. Bader. “A Quantum Theory of Molecular Structure and Its Applications”. In: *Chemical Reviews* 91.5 (July 1991), pp. 893–928. ISSN: 0009-2665. DOI: `10.1021/cr00005a013`.

[57] Julian Schwinger. “The Theory of Quantized Fields. I”. In: *Physical Review* 82.6 (June 1951), pp. 914–927. DOI: `10.1103/PhysRev.82.914`.

[58] G. K. H. Madsen et al. “F Center in Sodium Electrosodalite as a Physical Manifestation of a Non-Nuclear Attractor in the Electron Density”. In: *Physical Review B* 59.19 (May 1999), pp. 12359–12369. DOI: `10.1103/PhysRevB.59.12359`.

[59] Andreas Garhofer. “Ab Initio Studies of Graphene-Metal Interfaces”. en. PhD thesis. Vienna University of Technology, 2013.

[60] Hassan Raza, ed. *Graphene Nanoelectronics: Metrology, Synthesis, Properties and Applications*. en. NanoScience and Technology. Berlin Heidelberg: Springer-Verlag, 2012. ISBN: 978-3-642-20467-8. DOI: `10.1007/978-3-642-22984-8`.

[61] G. Kresse and J. Hafner. “Ab Initio Molecular Dynamics for Liquid Metals”. In: *Physical Review B* 47.1 (Jan. 1993), pp. 558–561. DOI: `10.1103/PhysRevB.47.558`.

[62] G. Kresse and J. Hafner. “Ab Initio Molecular-Dynamics Simulation of the Liquid-Metal–Amorphous-Semiconductor Transition in Germanium”. In: *Physical Review B* 49.20 (May 1994), pp. 14251–14269. DOI: `10.1103/PhysRevB.49.14251`.

[63] G. Kresse and J. Furthmüller. “Efficiency of Ab-Initio Total Energy Calculations for Metals and Semiconductors Using a Plane-Wave Basis Set”. en. In: *Computational Materials Science* 6.1 (July 1996), pp. 15–50. ISSN: 0927-0256. DOI: `10.1016/0927-0256(96)00008-0`.

[64] G. Kresse and J. Furthmüller. “Efficient Iterative Schemes for Ab Initio Total-Energy Calculations Using a Plane-Wave Basis Set”. In: *Physical Review B* 54.16 (Oct. 1996), pp. 11169–11186. DOI: `10.1103/PhysRevB.54.11169`.

[65] P. E. Blöchl. “Projector Augmented-Wave Method”. In: *Physical Review B* 50.24 (Dec. 1994), pp. 17953–17979. DOI: `10.1103/PhysRevB.50.17953`.

[66] G. Kresse and D. Joubert. “From Ultrasoft Pseudopotentials to the Projector Augmented-Wave Method”. In: *Physical Review B* 59.3 (Jan. 1999), pp. 1758–1775. DOI: `10.1103/PhysRevB.59.1758`.

[67] M. Methfessel and A. T. Paxton. “High-Precision Sampling for Brillouin-Zone Integration in Metals”. In: *Physical Review B* 40.6 (Aug. 1989), pp. 3616–3621. DOI: `10.1103/PhysRevB.40.3616`.

[68] Alpha T. N'Diaye et al. "Two-Dimensional Ir Cluster Lattice on a Graphene Moiré on Ir(111)". en. In: *Physical Review Letters* 97.21 (Nov. 2006), p. 215501. DOI: `10.1103/PhysRevLett.97.215501`.

[69] Alpha T. N'Diaye et al. "Structure of Epitaxial Graphene on Ir(111)". en. In: *New Journal of Physics* 10.4 (Apr. 2008), p. 043033. ISSN: 1367-2630. DOI: `10.1088/1367-2630/10/4/043033`.

[70] K. Momma and F. Izumi. "VESTA 3 for Three-Dimensional Visualization of Crystal, Volumetric and Morphology Data". en. In: *Journal of Applied Crystallography* 44.6 (Dec. 2011), pp. 1272–1276. ISSN: 0021-8898. DOI: `10.1107/S0021889811038970`.

[71] Ask Hjorth Larsen et al. "The Atomic Simulation Environment—a Python Library for Working with Atoms". en. In: *Journal of Physics: Condensed Matter* 29.27 (June 2017), p. 273002. ISSN: 0953-8984. DOI: `10.1088/1361-648X/aa680e`.

[72] Fabian Pedregosa et al. "Scikit-Learn: Machine Learning in Python". In: *Journal of Machine Learning Research* 12 (Oct. 2011), pp. 2825–2830. ISSN: 1533-7928.

[73] Matt Newville et al. *Lmfit/Lmfit-Py 1.0.1*. Zenodo. May 2020. DOI: `10.5281/zenodo.3814709`.

[74] Péter Pulay. "Convergence Acceleration of Iterative Sequences. the Case of Scf Iteration". en. In: *Chemical Physics Letters* 73.2 (July 1980), pp. 393–398. ISSN: 0009-2614. DOI: `10.1016/0009-2614(80)80396-4`.

[75] William H. Press et al. *Numerical Recipes 3rd Edition: The Art of Scientific Computing*. en. Cambridge University Press, Sept. 2007. ISBN: 978-0-521-88068-8.

[76] Graeme Henkelman, Andri Arnaldsson, and Hannes Jónsson. "A Fast and Robust Algorithm for Bader Decomposition of Charge Density". In: *Computational Materials Science* 36.3 (June 2006), pp. 354–360. ISSN: 0927-0256. DOI: `10.1016/j.commatsci.2005.04.010`.

[77] Edward Sanville et al. "Improved Grid-Based Algorithm for Bader Charge Allocation". en. In: *Journal of Computational Chemistry* 28.5 (2007), pp. 899–908. ISSN: 1096-987X. DOI: `10.1002/jcc.20575`.

[78] W. Tang, E. Sanville, and G. Henkelman. "A Grid-Based Bader Analysis Algorithm without Lattice Bias". en. In: *Journal of Physics: Condensed Matter* 21.8 (Jan. 2009), p. 084204. ISSN: 0953-8984. DOI: `10.1088/0953-8984/21/8/084204`.

[79] Min Yu and Dallas R. Trinkle. “Accurate and Efficient Algorithm for Bader Charge Integration”. In: *The Journal of Chemical Physics* 134.6 (Feb. 2011), p. 064111. ISSN: 0021-9606. DOI: `10.1063/1.3553716`.

[80] Philip M. Morse. “Diatomic Molecules According to the Wave Mechanics. II. Vibrational Levels”. In: *Physical Review* 34.1 (July 1929), pp. 57–64. DOI: `10.1103/PhysRev.34.57`.

[81] Gustav Mie. “Zur kinetischen Theorie der einatomigen Körper”. de. In: *Annalen der Physik* 316.8 (1903), pp. 657–697. ISSN: 1521-3889. DOI: `10.1002/andp.19033160802`.

[82] Mikael Rechtsman, Frank Stillinger, and Salvatore Torquato. “Designed Interaction Potentials via Inverse Methods for Self-Assembly”. In: *Physical Review E* 73.1 (Jan. 2006), p. 011406. DOI: `10.1103/PhysRevE.73.011406`.

[83] Michael Engel and Hans-Rainer Trebin. “Self-Assembly of Monatomic Complex Crystals and Quasicrystals with a Double-Well Interaction Potential”. In: *Physical Review Letters* 98.22 (June 2007), p. 225505. DOI: `10.1103/PhysRevLett.98.225505`.

[84] J. Friedel. “Metallic Alloys”. en. In: *Il Nuovo Cimento (1955-1965)* 7.2 (Sept. 1958), pp. 287–311. ISSN: 1827-6121. DOI: `10.1007/BF02751483`.

[85] H. C. Hamaker. “The London—van Der Waals Attraction between Spherical Particles”. en. In: *Physica* 4.10 (Oct. 1937), pp. 1058–1072. ISSN: 0031-8914. DOI: `10.1016/S0031-8914(37)80203-7`.

[86] Jacob N. Israelachvili. *Intermolecular and Surface Forces*. en. Third. Academic Press, 2011. ISBN: 978-0-12-391927-4. DOI: `10.1016/C2011-0-05119-0`.

[87] U. Hartmann. “Van Der Waals Interactions between Sharp Probes and Flat Sample Surfaces”. In: *Physical Review B* 43.3 (Jan. 1991), pp. 2404–2407. DOI: `10.1103/PhysRevB.43.2404`.

[88] Lina Kulakova et al. “Data Driven Inference for the Repulsive Exponent of the Lennard-Jones Potential in Molecular Dynamics Simulations”. en. In: *Scientific Reports* 7.1 (Nov. 2017), p. 16576. ISSN: 2045-2322. DOI: `10.1038/s41598-017-16314-4`.

[89] Guillaume Galliéro et al. “Molecular dynamics comparative study of Lennard-Jones α-6 and exponential α-6 potentials: Application to real simple fluids (viscosity and pressure)”. In: *Physical Review E* 73.6 (June 2006), p. 061201. DOI: `10.1103/PhysRevE.73.061201`.

[90] Massimiliano Bonamente. *Statistics and Analysis of Scientific Data*. en. Second. Graduate Texts in Physics. New York: Springer-Verlag, 2017. ISBN: 978-1-4939-6570-0. DOI: `10.1007/978-1-4939-6572-4`.

[91] Changgu Lee et al. “Elastic and Frictional Properties of Graphene”. en. In: *physica status solidi (b)* 246.11-12 (2009), pp. 2562–2567. ISSN: 1521-3951. DOI: 10.1002/pssb.200982329.

[92] Changgu Lee et al. “Frictional Characteristics of Atomically Thin Sheets”. en. In: *Science* 328.5974 (Apr. 2010), pp. 76–80. ISSN: 0036-8075, 1095-9203. DOI: 10.1126/science.1184167.

[93] Kenneth Levenberg. “A Method for the Solution of Certain Non-Linear Problems in Least Squares”. en. In: *Quarterly of Applied Mathematics* 2.2 (1944), pp. 164–168. ISSN: 0033-569X, 1552-4485. DOI: 10.1090/qam/10666.

[94] Donald W. Marquardt. “An Algorithm for Least-Squares Estimation of Nonlinear Parameters”. In: *Journal of the Society for Industrial and Applied Mathematics* 11.2 (June 1963), pp. 431–441. ISSN: 0368-4245. DOI: 10.1137/0111030.

[95] Rene Andrae. “Error Estimation in Astronomy: A Guide”. In: *arXiv:1009.2755* (Sept. 2010). arXiv: 1009.2755.